INVESTIGATION OF THE LATERAL BUILDUP RATIO USED FOR SMALL OR IRREGULAR FIELD ELECTRON DOSIMETRY

By

Dallin Francom

A THESIS

Presented to the Department of Medical Physics
and the Oregon Health & Science University
School of Medicine
in partial fulfillment of
the requirements for the degree of

Master of Science

June 2019

SCHOOL OF MEDICINE

OREGON HEALTH & SCIENCE UNIVERSITY

CERTIFICATE OF APPROVAL

This is to certify that the Master's thesis of

Dallin Francom

has been approved

_____	_____
Date	Richard J. Crilly, Mentor/Advisor
_____	_____
Date	Susha Pillai, Committee Member
_____	_____
Date	Lindsay DeWeese, Committee Chair

Table of Contents

List of Tables

List of Figures

Acknowledgements

I would like to express my gratitude to the outstanding medical physicists at Oregon Health & Science University for being such great resources and always keeping their doors open for questions. They not only simply answered questions, but often helped me to figure out the answers or worked with me if the solutions were unknown.

I would also like to thank Dr. Rick Crilly for guiding me in the preparation for two separate projects. Despite his involvement in so many other projects and clinical tasks he still made ample time to guide me through the course of this project. Thank you for your patience with me, and for providing your mentorship.

Next I would like to thank the all professors of the medical physics program at OHSU. Their preparation and time put into lectures went a long way in helping me be prepared for the ABR and interviews.

Lastly, I would like to thank my patient and loving wife Saraiah. She has been the foundation for me to be able to do any of this work. She has always been patient, understanding, and encouraging to me at all times. I could not have done my graduate work without her support. Also, a thank you to my children who always made going home an excitement, and for greeting me with a hug.

Abstract

Purpose: To verify the accuracy of the lateral buildup ratio (LBR) proposed in TG-70 for the dosimetry of electrons with small or irregular fields and investigate an alternative measurement used for the LBR.

Methods: The theory proposed in TG-70 uses the LBR as a main concept for small field calculations. The LBR is a ratio of percent depth dose (PDD) profiles from a small circular field and a 'broad field', which is then incorporated into an electron pencil-beam model. This method claims to result in calculated output factors that agree within $\pm$3% at clinically significant depths. To facilitate this test, two Cerrobend cutouts were made for a 25 cm^2 cone using 3D-printed cylinders to define the hole size in the mold. In addition to the suggested 2 cm cutout, a 1 cm cutout was made to investigate the LBR produced and its effect on the electron pencil-beam model. Electron energies of 6, 8, 10, 12, and 15 MeV were considered from an Elekta Versa HD. Circular cutouts of 2, 3, 4, 8 cm and an irregular field were made and depth profiles measured to compare with theoretical calculations.

Results: The LBRs were created for both the 2 cm and 1 cm cutouts, and incorporated into two individual pencil-beam parameters σ_{2cm} and σ_{1cm}, respectively. These were used individually to calculate circular and irregular field sizes for all energies. The profiles were analyzed at d_{max} and R_{90} to reflect clinically significant depths.

Conclusion: The calculations from σ_{2cm} for all fields, including the irregular field, better matched the measured values when compared to the σ_{1cm} calculations. For energies at 10 MeV and below, the σ_{2cm} calculation stayed within 3% of the measured dose at R_{90} for all cutouts. The calculations

from the σ_{1cm} parameter varied by as much as 9% of the measured dose at R_{90} for 10 MeV, occurring with the 2 cm cutout. For all cutouts and energies, the calculations from σ_{2cm} produced data closer in depth and percentage of dose to measured d_{max} and R_{90} values.

Chapter 1

Introduction

The purpose of this thesis is to validate the lateral buildup ratio (LBR) originally proposed by Kahn[1] and to test a modified approach. In order to facilitate this study, an Elekta Versa HD linear accelerator was used, which is commissioned for both photon and electron treatments. At the start of this work, OHSU did not have a stand-alone calculation book of standard electron cutouts. Also, there is no second-check method of calculating small or irregular cutouts other than physical cutout measurements. In 1998, Kahn proposed a simplified method of making such calculations for electrons.[1] Various investigators have assessed the accuracy of this method.[2–7] The purpose of this thesis was to investigate the effects of using an alternative measurement for the LBR, in addition to the overall acceptability of the method.

In the United States, it is estimated that more than 1.7 million people will be diagnosed with cancer during the year 2019. Also in the United States, an estimated 606,880 people will die from cancer.[8] Many cancer cases can be treated with linear accelerator based electrons fields due to their unique dosimetric properties. Electron fields exhibit a relatively high surface dose, a near uniform dose plateau at depths of maximum dose, and a steep dose fall off. Thus skin or near surface cancers are typically good candidates for being treated with electron therapy. The steep fall off of dose from electrons help to minimize dose to critical structures distal to the treatment site. The fields, or dimensions, necessary for adequate collimation are often irregular or small and thus will change the dose profile delivered by electrons.[9] What is written hereafter will address these complications to planning strategies and explain the methods used.

1.1 Electron Therapy

With the discovery of x-rays occurring in late 1895 by W. C. Roentgen, an immediate application of using x-rays in medicine began.[10] Initially, the direct application of the x-rays were for diagnostic purposes. However, the therapeutic use of radiation followed within months.[10] The use of radiation for medicinal purposes was also extended to particulate radiation. Electrons thus became a tool for the treatment of cancers and other diseases.

Electrons are successfully implemented and used for certain disease types, including cancer, and locations usually near a surface. Some of these diseased sites are the scalp, nose, ear, eye, eyelid, neck nodes, breast, extremities, spinal cord, posterior chest wall, total skin (in cases of Mycosis Fungoides),[11] and intraoperatively for the pancreas, cervix, and other sites.[12,13]

1.1.1 Historical Use

External electron beam therapy began around the late 1930's in a device called the Van de Graaff generator which was built by Van de Graaff and Trump.[14] The Van de Graaff generator has a conveyer belt that is loaded with electrons, which are then transmitted onto a conductor. The conductor is attached to a filament, which leads to an accelerating structure towards ground potential. The electron energies produced from these units are limited to about 2 – 3 MeV. Soon after the invention of the Van de Graaff accelerator, the unit was implemented clinically for the treatment of cancer.[15,16]

Following the Van de Graaff generators, Betatrons were created about a decade later with energy capabilities between 6 and 30 MeV. These units assumed a more active role in the clinic, however was limited due to their size and bulk.[17] An image of a Siemens Betatron 42 being used

in the clinic can be found from the University of Saskatchewan, University Archives & Special Collections, MG 372, Harold Johns fonds, Negatives, Betatron-42, 1972. About this time, linear accelerators were being introduced to replace orthovoltage x-ray units with sources of higher energy photons. These 'linacs' were readily engineered to allow the delivery of high energy electron beams as well.

1.1.2 Current Clinical Use

In a typical modern linear accelerator the electrons are stripped off of a filament, called the electron gun, by thermionic emission. The electrons are accelerated to about one-fourth of the speed of light by a pulsed direct current (DC) electric field towards an aperture on the anode and are then bunched into the accelerating tube.[18] After leaving the electron gun, microwaves created in the magnetron are sent to the accelerating tube to further accelerate the electrons. At times a klystron may be used to further amplify the microwave output to the accelerating structure. The accelerating tube is typically 1 – 2 meters in length and at its end is the treatment head of the unit. In the head of the linear accelerator the electron beam is bent, broadened, and flattened. Modern linear accelerators are capable of rotation around the patient. To allow for this capability, it is necessary to bend the beam towards the treatment direction which is typically perpendicular to the accelerating tube. The strength of the magnetic fields must be variable to converge the electrons to the same point, regardless of electron energies being selected. For Elekta units the electrons are typically bent in a slalom fashion, totaling about 112.5°, and then are converged back to a point. The electrons are mostly monoenergetic and confined to a small beamlet, or pencil beam. If photons are desired, a thin target of high Z material, usually tungsten, is put in place to interact with the electrons and create photons via bremsstrahlung radiation. If electrons are desired, a scattering foil is put in place which broadens the fine electron beam. Usually either a secondary

central or annular foil is in place to help flatten the Gaussian spread of the electrons from the primary foil. Two ionization chambers are set in the treatment head of the beam for measuring and monitoring of the radiation being delivered. Primary and secondary collimations are not quite in place at the field edge for electron beams because the electrons will scatter off the collimators and cause an increase in scattered radiation to the patient, as well as an increase in the geometric penumbra. Figure 1 demonstrates the dose changes that occur when the photon jaw settings are varied for electron fields. This also displays the sensitivity electrons exhibit due to collimation in the treatment head, particularly for lower energies.[19] Notice that if the photon jaws are set to the field size of the cone, the 10 × 10 cm, the dose decreases by about 40% for the 4 MeV electron beam.

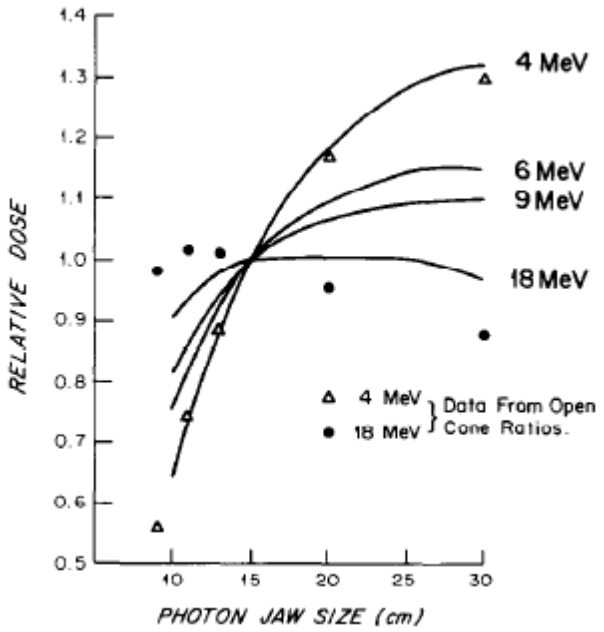

Figure 1. This shows how vastly the relative dose from electrons can change by adjusting the photon collimation jaws. Reprinted from International Journal of Radiation Oncology*Biology*Physics, Vol 5 Issue 3, Peter J. Biggs, Arthur L. Boyer, Karen P. Doppke, Electron dosimetry of irregular fields on the clinac 18, 433-440, Copyright (1979), with permission from Elsevier.

The collimators are thus adjusted to be mostly out of the beam depending which cone, or electron applicator, is being used. These electron cones are attached to the head of the linear accelerator. These events are shown in Figure 2.

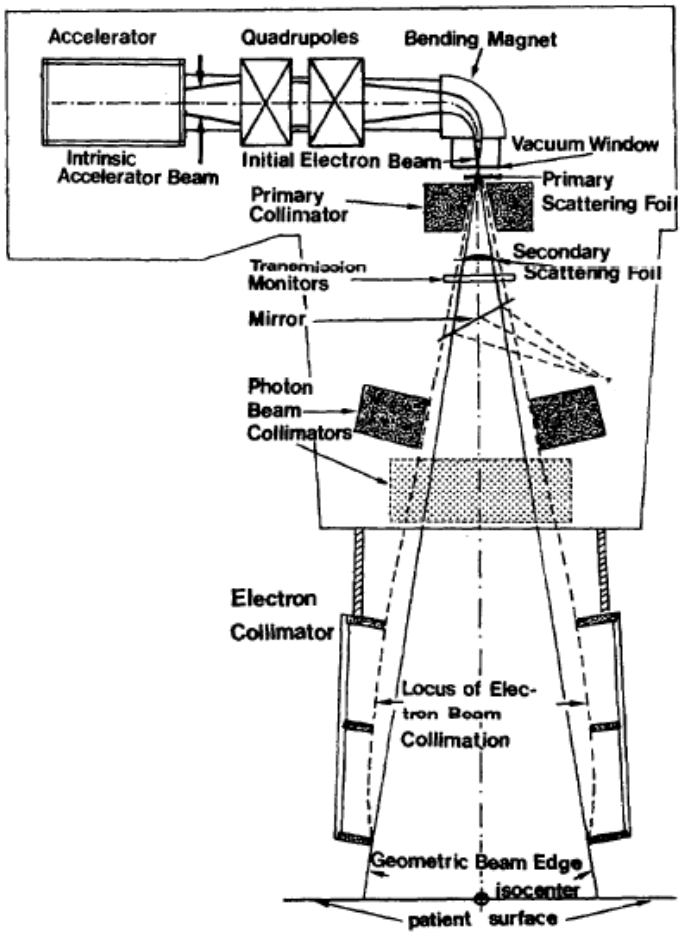

Figure 2. A diagram of the head of a modern medical linear accelerator. This image represents the accelerator being used in the electron mode. Reproduced with permission of the International Commission on Radiation Units and Measurements, http://ICRU.org

The electron cones continue to shape the electrons in a series of collimations. The purpose of the open collimation is to reduce electron scatter into the clinical beam, as shown in Figure 3. The series of collimators are intended to reduce the penumbra produced from the upstream collimation up to the 95% of the upstream profile intensity[20] (see Figure 4). At the bottom of these

cones the user can attach further patient specific collimation. These patient specific collimations are referred to as cutouts. It has been found that when individual cutouts are used there is no significant perturbation of the incident electron spectrum.[21]

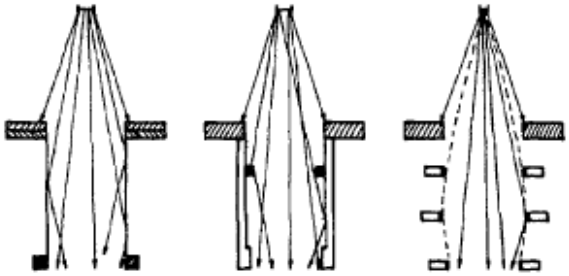

Figure 3. The purpose of the open electron cone is to reduce scatter radiation into the beam when compared to other types of collimation shown on the left. Reproduced with permission of the International Commission on Radiation Units and Measurements, http://ICRU.org

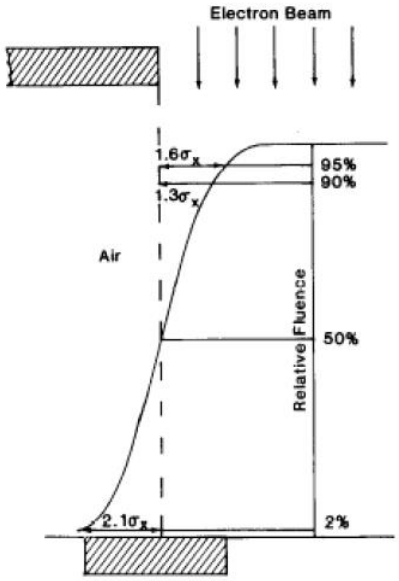

Figure 4. This represents the electron beam intensity being blocked by the electron cone. Reprinted from International Journal of Radiation Oncology*Biology*Physics, Vol 18 Issue 5, K. R. Hogstrom, A. L. Boyer, A. S. Shiu, T. G. Ochran, S. M. Kirsner, F. Krispel, Tyvin Rich, Design of metallic electron beam cones for an intraoperative therapy linear accelerator, 1223-1232, Copyright (1990), with permission from Elsevier.

1.1.3 Dosimetric Properties of Electrons

Figure 5 shows the generic profile for a mega electron volt energy range electron beam. Also shown are some parameters commonly used when referring to or comparing electron profiles.

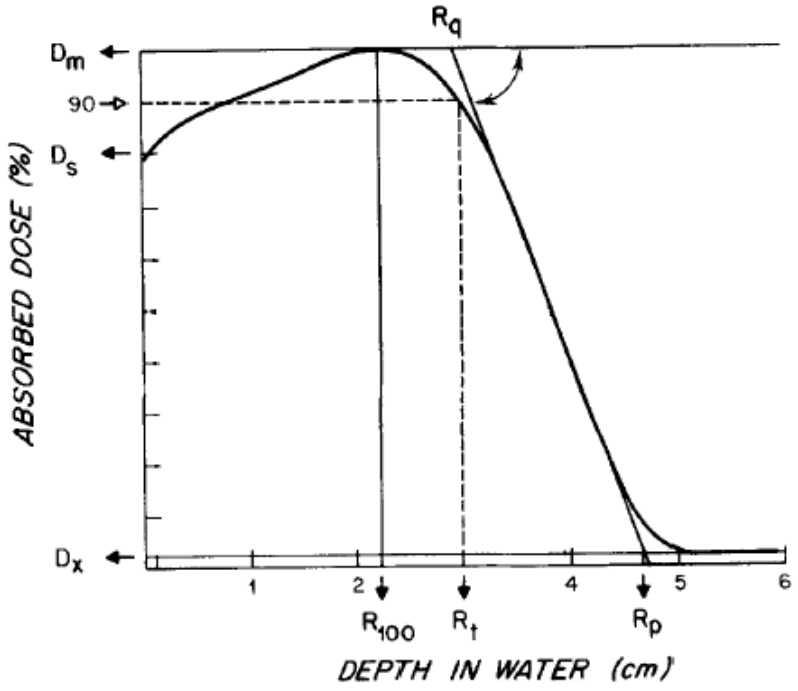

Figure 5. A profile for an MeV electron central axis profile, featuring clinical points of interest. Adapted from "Clinical electron-beam dosimetry: Report of AAPM Radiation Therapy Committee Task Group No. 25," by Khan FM, Doppke KP, Hogstrom KR, et al. Copyright 2009 by American Association of Physicists in Medicine. Reprinted courtesy of the American Association of Physicists in Medicine under a Creative Commons License CC By 3.0

D_s is the dose at the surface of the phantom, R_{100} is the depth of maximum dose deposition and is commonly referred to as d_{max}, R_{90} is the distal depth where 90% of the maximum dose is deposited and is referred to as the therapeutic range or the clinically useful depth, R_p is the practical

range of the electron, and R_q is "the depth at which the tangent to the curve at the point of inflection meets the level of d_{max}".[22]

Electrons exhibit a higher entrance dose than photons, and have a minimal skin-sparing effect. Because of their charge and small mass, the electrons start interacting with the phantom material through scattering and energy transference. Lower energy electrons are more likely to scatter at wider angles. This broad scatter leads to a rapid buildup of dose closer to the surface. As the energy of electrons increases, the entrance dose also increases due to the lack of lateral scatter to increase the dose at depth. Electrons at higher energies are more forward-scattered and give the percent depth dose (PDD) profile a more broad shape with a higher relative entrance dose.[9] The electron profiles for different energies are shown in Figure 6.

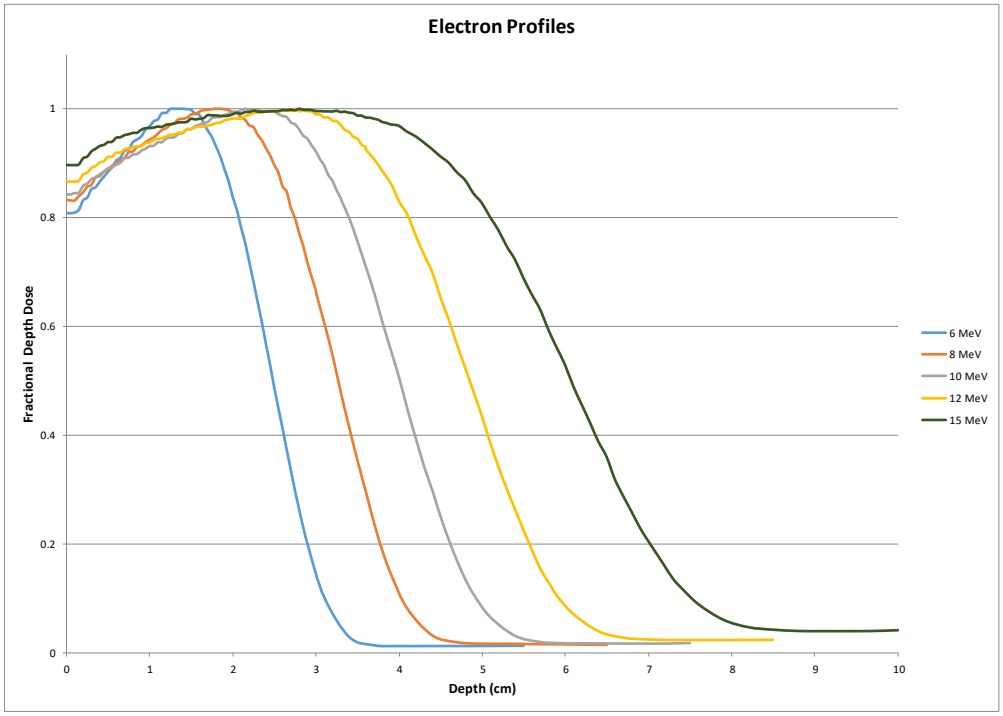

Figure 6. Electron profiles for five different electron energies.

When considering a point in an electron beam at some depth along the central axis, upstream electrons that should have scattered into the point of consideration are scattered out and are not detected. On the other hand, electrons that might not have been in line to interact in the point of consideration might scatter into the point, and are detected. When the amount of electrons scattering in are approximately equal to the same amount of electrons scattering out, a condition arises called lateral scatter equilibrium (LSE). When LSE is met, the PDD of the electron beam becomes roughly independent of field size. At field sizes less than what is required for LSE, the PDD of the electron beam becomes dependent on field size, the dose rate decreases, and the output (dose per monitor unit (MU)) decreases.[9] Authors Khan and Higgins[23] estimated that the radius requirement for LSE is given by Equation 1,

$$R_{eq} \cong 0.88\sqrt{E_{p,0}} \tag{1}$$

where R_{eq} is in cm and $E_{p,0}$ (MeV) is the most probably energy at the surface of a phantom. $E_{p,0}$ is derived and calculated as an empirical equation by Nordic Association of Clinical Physics,[24] given as

$$\left(E_p\right)_0 = C_1 + C_2 R_p + C_3 {R_p}^2 \tag{2}$$

where R_p is the practical range of the electrons as described earlier, and the coefficients C_1, C_2, and C_3 are $0.22\ \text{MeV}$, $1.98\ \text{MeV/cm}$, and $0.0025\ \text{MeV/cm}^2$, respectively. Accordingly, for larger field sizes and energies, the PDD profiles maintain a nearly similar shape to those just above the LSE required radius. This relationship is detailed in Figure 7. Once the radius required for LSE is not met, the PDD decreases, d_{max} moves closer to the surface, and surface dose increases.

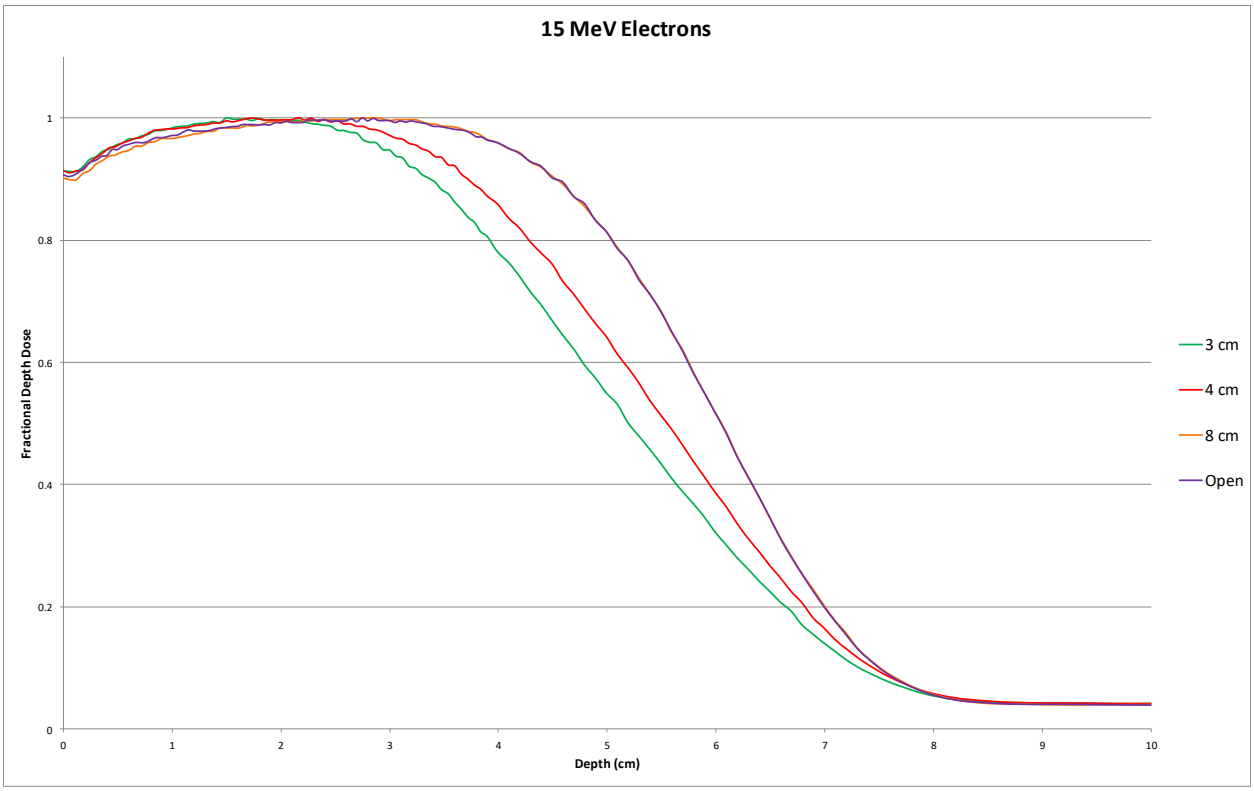

Figure 7. Graphed is the dependence of the electron profile on field size. Note that changing the field size from 8 cm to the open cone barely changes the profile and the two are hardly distinguishable. Measurements were taken in a 10 x 10 cm cone.

It is important to note that most prescriptions are given with respect to the R_{90} depth. However, if that depth is based off an incorrect field size then an inaccurate dose could be delivered. It is important to understand that the electron profiles change drastically for small or irregular field sizes, and must be taken into consideration when prescribing dose to patients.

1.2 Small/Irregular Field Calculation Methods

1.2.1 Algorithmic Methods

In the past, many electron dose algorithms used empirical methods and functions based on an assumed a broad beam distribution. Furthermore, they assumed that electrons traversed through

homogeneous material, and used ray line geometries.[25] Later, around the 1980's, methods utilizing pencil beams to calculate dose distributions for electron fields emerged.[26,27] These use multiple scattering theory to predict and generalize the dose deposition of electrons. The pencil beam theory is based on the premise that the electron spread is axially uniform and follows a Gaussian spread. Algorithmic methods use many pencil beam parameters to calculate the electron scatter in a 2D surface convolution. Jursinic and Mueller analyzed and compared different methods proposed for calculating electron output factors, and are summarized in Figure 8.[4]

Calculation method	Percentage difference ($\leq \pm$ %)
Equivalent square	2.7,[a] 5.9,[b] 3.0[c]
Square root	3.0,[d] 2.3,[e] 4.6,[b] 3.0[f]
One dimensional	3.0,[d] 2.0,[e] 2.1[b]
Pencil beam	2.7,[g] 2.0[h]
Sector integration	3.0,[i] 1.5,[j] 1.0,[k]

Figure 8. Various calculation methods used for electron dosimetry are evaluated based on their percentage difference between measured and calculated output factors. The superscripts used are references to other publications. For further information see Task Group 70, "Recommendations for clinical electron beam dosimetry: Supplement to the recommendations of Task Group 25". Copyright 2009 by American Association of Physicists in Medicine. Reprinted courtesy of the American Association of Physicists in Medicine under a Creative Commons License CC By 3.0

Monte Carlo methods are currently employed for Elekta units in a treatment planning system (TPS) called Monaco® for both electrons and photons. Experimental studies have evaluated the accuracy of these calculations and found that the measured dose and output factors for fields ranging down to 3 cm diameter agree with the electron Monte Carlo (eMC) calculations within ± 2.5%. The profiles also agree within 2.5% or 2 mm at locations of d_{max} and R_{90}.[28]

Despite the accuracy of current eMC methods it is always necessary to have a second-check to compare to the primary calculation. Currently at OHSU, when small and/or irregular electron cutouts are encountered the outputs are measured individually for direct calibration.

1.2.2 Khan's Method

In the paper by Khan et al, a method is proposed to calculate the depth profiles for electrons from small or irregular fields. The key concept is the use of the lateral buildup ratio (LBR), which is the "ratio of dose at a point at depth for a given circular field to the dose at the same point for a 'broad-field', for the same incident fluence and profile." The mathematical expression for the LBR is shown in Equation 3.

$$LBR(R,z,E) = \frac{D(R,z,E)}{D(R_\infty,z,E)}\frac{\Phi_i(R_\infty,E)}{\Phi_i(R,E)} \tag{3}$$

This method is applied to a pencil beam model, where the electron spread is approximated as Gaussian. Thus the LBR is related to the pencil beam parameter, σ_r, and is due to multiple Coulomb scattering. The relation between the LBR and σ_r is shown in Equation 4.

$$LBR(R,z) = 1 - \exp(-R^2/\sigma_r^2(z)) \tag{4}$$

$\sigma_r^2(z)$ is the mean square radial spread as a function of depth, which defines the electron spread.

The small circular field to create the LBR is suggested to be a 2 cm diameter cutout. The reasoning for this specific diameter is if larger diameters are used, then LSE might still not be met at higher electron energies, rendering this method ineffective for modeling the electrons. The only reference against using a smaller circular cutout is the difficulty of measurement. The hypothesis is that a better ratio would be obtained with an even smaller diameter and thus provide a more

accurate calculation. With the pencil beam being calculated, the LBR for any circular radius can be calculated. For calculation of an irregular shaped field a sector-type integration method is done (see Equation 7 in the following Chapter for details).

1.3 Aim of the Study

The purpose of this thesis is to verify the accuracy of the LBR method proposed by Khan et al. In addition, an alternative measurement of a 1 cm diameter cutout for calculating the LBR is explored to assess the viability of producing more accurate calculations. In concept this smaller cutout would better match the principle of the LBR; a ratio of having little to no electron scatter versus ample electron scatter. It is also anticipated that the calculations will be set up in a way that will allow for an easy recalculation of various fields.

Chapter 2

Methods

The set up and methodology of data collection to create the LBR is described in this chapter. The layout of the Excel Book is also described. Also in this section is a description of how data was collected for the comparison between measured and calculated PDDs. Lastly, the calculations used to create the depth profile for an irregular field is also described, as well as its comparison to the measurement.

2.1 Measuring the Lateral Buildup Ratio

As previously described in section 1.2.2, the lateral buildup ratio (LBR) is the depth matched ratio of PDDs between a small field and a large field. Khan et al suggests that the small field be a circular cutout of 2 cm diameter[1]. In addition to this cutout a 1 cm cutout was also made as an attempt to better match the underlying logic of the LBR, which is essentially a ratio of minimal scattered electrons to that of an electron beam with full lateral equilibrium. Attempting to nullify any other source of variability due to using different cones, a 25 cm × 25 cm cone was chosen for the broad field as well as the small field. This was to negate slight effects caused by using a different cone for these measurements. It has been found that when larger cones are used, the R_{90} is shifted deeper than when a smaller cone is used for the same field size. It is assumed this result is due to low-energy x-rays that are scattered off the applicator and jaws for the smaller cones compared to the larger cones.[29]

To ensure an accurate cutout, cylinders of diameters 1 cm and 2 cm were printed using an Ultimaker 2 3D printer. Their design was created using the software Tinkercad™. The files were printed using acrylonitrile butadiene styrene (ABS) filament. This filament was selected because of its availability in the clinic.

Cerrobend was used to create the necessary cutouts in the Department of Radiation Medicine's block room. Cerrobend is a eutectic alloy; a mixture of bismuth, lead, tin, and cadmium. It is an attractive material for radiation therapy due to its low melting temperature, high Z, and low cost. Previous studies have examined the dose due to transmission through the Cerrobend cutouts and found the minimal thickness of these cutouts to be about 16 mm for the highest energy beams encountered in radiation therapy.[30] The cylinders were placed in the middle of the holder and clamped down and the liquid Cerrobend was poured in the 25 cm x 25 cm holder. As seen in Figure 9 the holes were centered within the mechanical limitations of the mold system. It should be noted that the alignment was always verified before measurements were taken and the cutout's center was congruent with the center of the detector.

Figure 9. The cutouts created for the measurement of the LBR. The 3D printed cylinders were lined closely to the center.

Central axis depth profiles were measured in a 1D Scanner model 1233 (Sun Nuclear Corporation). The internal dimensions are 35 cm × 39 cm, with a depth of 35 cm. The configuration for measurements are shown in Figure 10.[31]

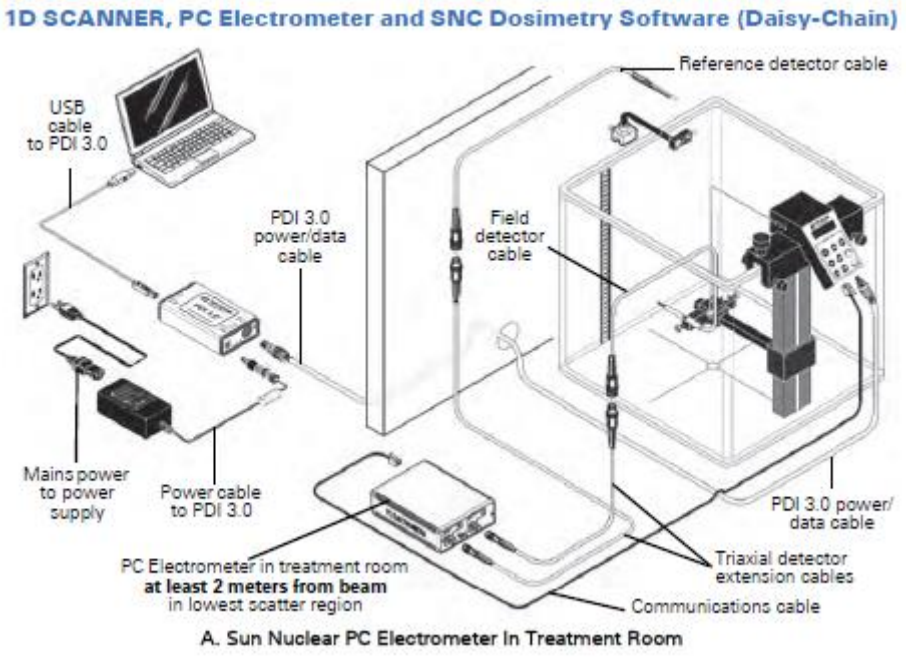

Figure 10. Set up of the 1D Scanner, electrometer, detectors, and the SNC software. 1D Scanner Reference Guide. Scanning Model 1233. With permission from SNC.

The detector used for all measurements was a PTW microDiamond detector (60019). This detector has an active volume of 0.004 mm^3 which is located 1 mm below the detector tip. The microDiamond was chosen because its small active volume makes it ideal for small field sizes. It is also water proof, and ideal for electron dose measurements.[32] The measurements also had a reference detector placed in the field on the first section of the cone. This was placed on the cone to be outside of the field incident on the cutout. The reference detector was a Dosimetry Diode E (60012). The Diode E has an active volume of 0.03 mm^3 with the volume located 1.33 mm from

the detector tip.[32] Both detectors were connected to a Sun Nuclear PC Electrometer. The software used was SNC Dosimetry, Version 3.5.0.19215, © Sun Nuclear 2019, Sun Nuclear Corporation. At the time of this data collection the full access to the software was not available, so the data was exported directly into Excel. Background measurements were taken before any other sets of measurements were recorded. The dwell time was set to 0.4 seconds per position and a point spacing of 0.1 cm. The maximum depth of the detector in the water was determined by the approximate value of the R_p value for the electrons. Clearly, this total scan depth varied for each electron energy. The source to surface distance (SSD) was set to 100 cm. The diode was verified to be centered along the cutout's center for depths up to 20 cm for each cutout. The profile data was left unaltered and imported into Excel for further work.

2.2 Calculating the Lateral Buildup Ratio

The electron measurements from each cutout were imported into Excel. The profiles were noticeably noisy, especially in regions near the surface. This is due to a rapid buildup region that can vary the signal, and also assumed because of the slight movement of water due to the moving diode and detector holder. It was necessary to smooth the data to avoid any major fluctuations in the LBR. The raw data was smoothed by averaging three measured dwell positions. This process was sufficient to smooth the profiles, as seen in Figure 11. The profiles were also normalized to 0.983 mm. By normalizing to this shallow depth, the incident fluence becomes the same for all field sizes regardless of cones being used. It has been shown that the acceptable depth for this to occur is between 0.5 mm – 3 mm. The depth of 0.983 mm was chosen because it was the first depth of measurement for all energies in the specified range with the up-beam non-sensitive part

of the detector at the water surface. By normalizing the profiles to the surface, the LBR from Equation 3 now becomes

$$LBR(R,z,E) = \frac{D(R,z,E)}{D(R_{\infty},z,E)} \tag{5}$$

Figure 12, Figure 13, and Figure 14 show the smoothed and normalized profiles.

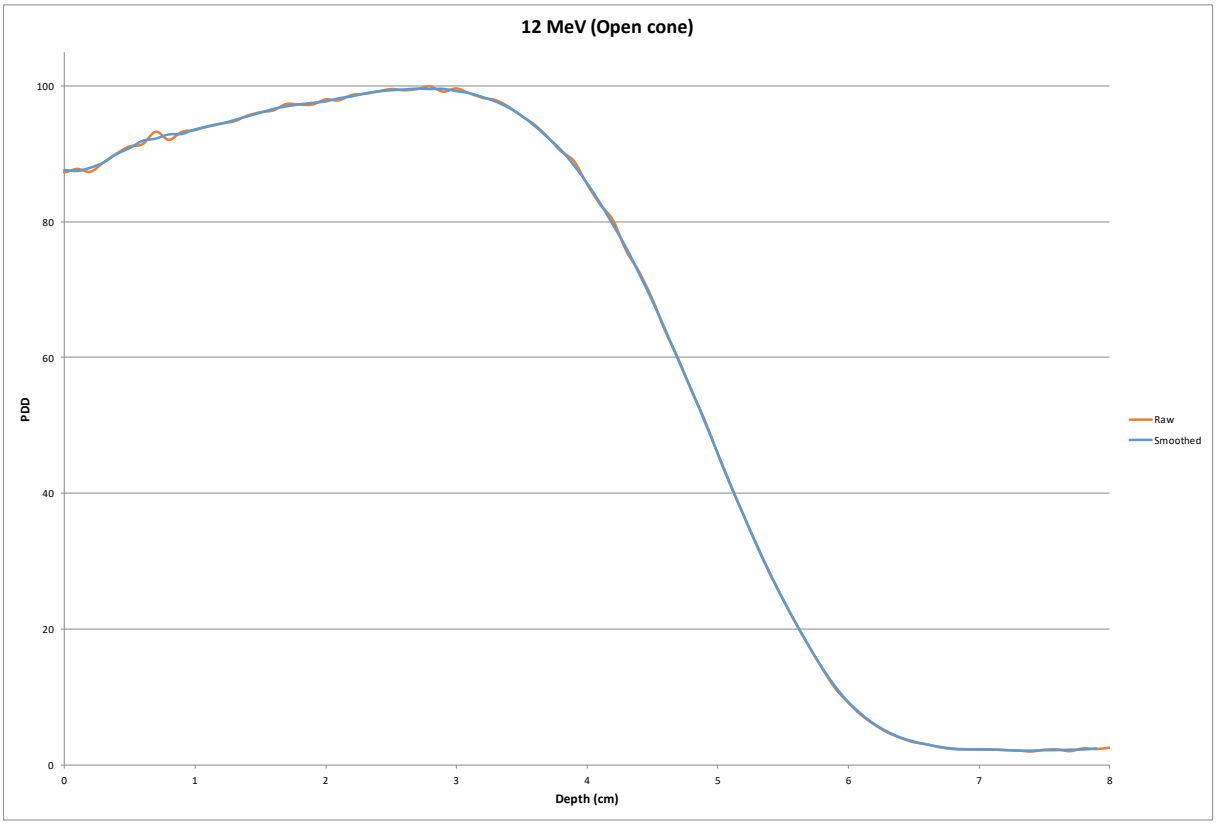

Figure 11. Depth profile from a 12 MeV electron beam in an open 25 cm^2 cone. Graphed is the raw data as well as the smoothed data for comparison.

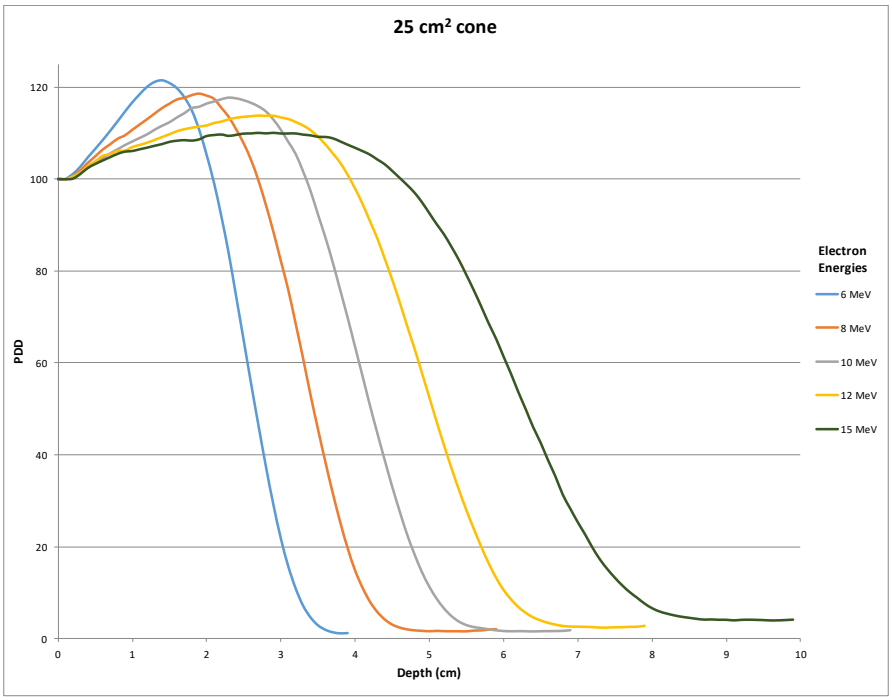

Figure 12. Smoothed and normalized depth profiles for all energies in an open 25 cm^2 cone.

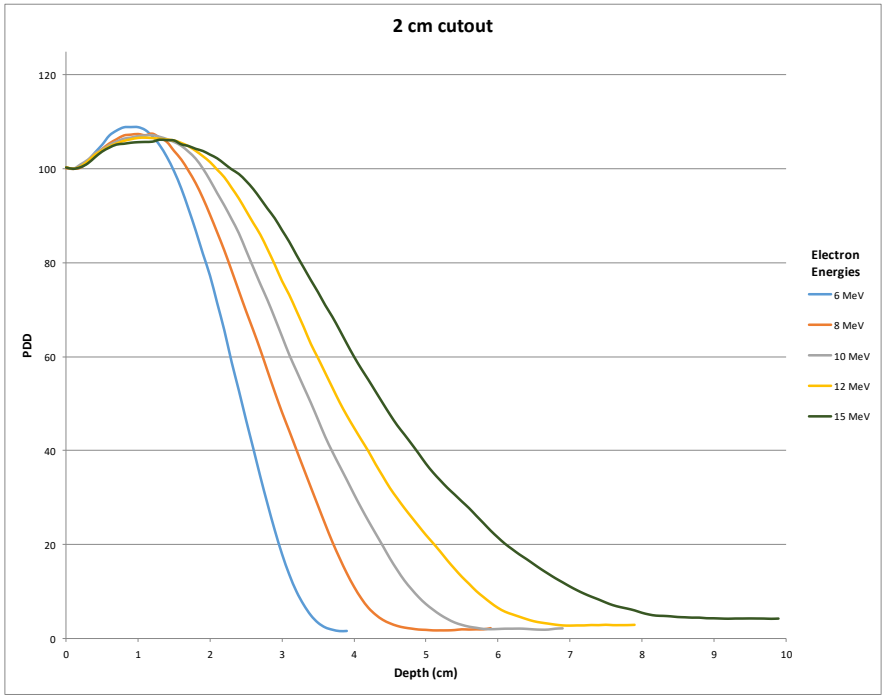

Figure 13. Depth profiles obtained from the 2 cm cutout for all energies. The data is smoothed and normalized to the surface.

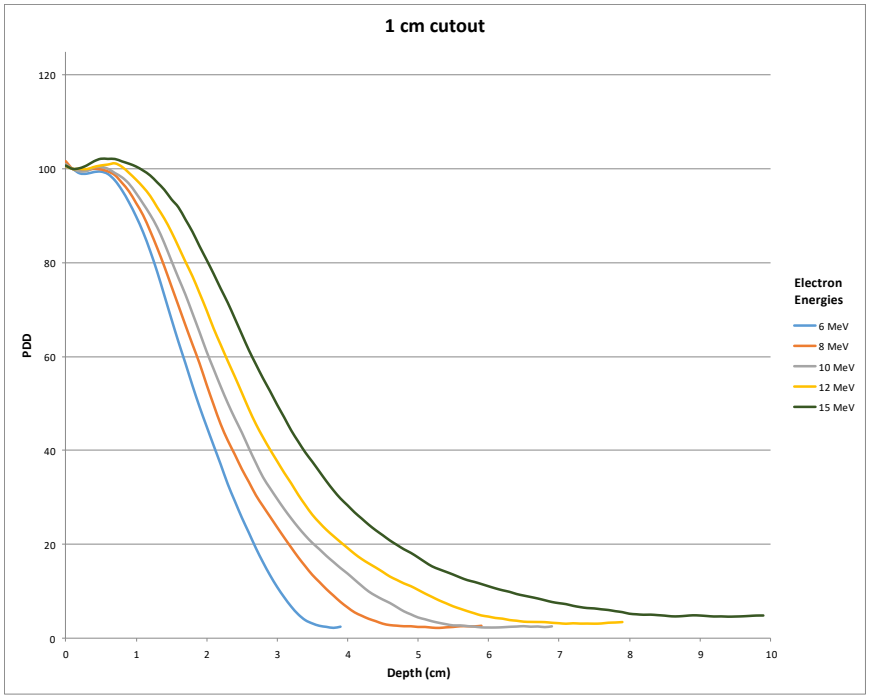

Figure 14. Depth profiles obtained from the 1 cm cutout for all energies. The data is smoothed and normalized to the surface.

The respective pencil beams were calculated for all depths using Equation 6

$$\sigma_r(z) = \frac{R}{\sqrt{\ln\left(\frac{1}{1 - LBR(R,z)}\right)}} \tag{6}$$

where R is the radius of a circular field size used to obtain the LBR. The LBR method as suggested in Task Group 70 uses one pencil beam, which is proposed to be sufficient for all other calculations. The justification for only using on parameter is that rather than being solely a computational approach, this method considers a Gaussian parameter from a measurement. Thus, this study utilized two pencil beam parameters, $\sigma_{1\text{cm}}$ and $\sigma_{2\text{cm}}$. Other work has shown that using

one pencil beam parameter might be insufficient.[5] It is also important to note that for this work the pencil beam parameters are labelled by their diameter. The parameter $\sigma_r(z)$ uses the radius.

With the pencil beam parameters calculated, the LBR for any radius can subsequently be calculated by using Equation 4. Each electron energy was calculated up to 8 cm diameter circular fields. Around 6 cm, the calculated LBR values for all electron energies started to become essentially one. This is expected because the LSE radius is nearly met for all the energies at this diameter. The LBR for various radii around an irregular field can then be incorporated into Equation 7 for the dose per monitor unit at point P,

$$D_u(P) = K(E) \cdot PDD(R_0, z, E) \cdot J(R_c, E) \cdot \frac{\Delta\theta}{2\pi} \sum_{i=1}^{n} LBR(R_i, z, E) \sum_{i=1}^{n} I(R_{i,c}, E) \qquad (7)$$

where $K(E)$ is the dose per MU for the 25 cm^2 cone at d_{max}, $P(R_0, z, E)$ is the PDD for the 25 cm^2 and is normalized to d_{max}, $J(R_c, E)$ is the cone factor and is equal to the incident fluence for the given cone of size R_c relative to the 25 cm^2 cone, $I(R_{i,c}, E)$ is the cutout factor. As stated earlier, a sector integration method is used to calculate the LBR at intervals of $\Delta\theta$, measured in radians. Equation 7 can further be reduced by considering that $J(R_c, E)$ and $\sum_{i=1}^{n} I(R_{i,c}, E)$ do not change the normalized depth dose distribution and are consequently factored out in the normalization.[5] For the circular cutouts, the summed LBR (referred to as the effective LBR (LBR_{eff}) in Task Group 70) reduces to the LBR. Thus, the terms reduce down to leave,

$$S_e(z, R) = S_e \cdot LBR_{\text{eff}} \cdot PDD(z, R_\infty) \qquad (8)$$

where

$$LBR_{\text{eff}}(z,R) = 1 - \left(\frac{\Delta\theta}{2\pi}\right)\sum_{i=1}^{n} \exp\left[\frac{-r_i^2}{\sigma_r^2(z)}\right] \quad (9)$$

and S_e is the cone factor.

The LBR for the irregular field was calculated using Equation 9. The irregular field was divided into 32 segments, and code was written in VBA to output the varying radii. LBR_{eff} was then calculated for all energies at all depths using both the σ_{1cm} and the σ_{2cm} parameters. This same calculation was performed from the corner of the irregular field. Once the LBR or LBR_{eff} is calculated, the dose per monitor unit for any field at any depth can be found using Equation 8.

2.3 Comparison Measurements

Measurements were taken for comparison to our calculated data. The cutouts and cones that were used are summarized in Table 1.

Table 1. The cutouts and their respective cones used to gather data for comparison with calculations.

6 cone	10 cone	14 cone
2 cm	3 cm	Irregular (center)
4 cm	4 cm	Irregular (corner)
	8 cm	

All of these cutouts, with the exception of the irregular field, were made previously. The set up was the same as described in section 2.1. The scan parameters were changed to a varying step size of 0.06 cm for locations shallower than d_{max}, 0.10 cm for depths between d_{max} and R_p, and 0.30 cm for depths greater than R_p. The dwell time was set to 1 second. Full access to the SNC software was available at the time that these measurements were taken. This would have made for an easier smoothing and normalizing of the data, however the smoothing mechanisms were

unclear. To be consistent, the data was imported directly into Excel and smoothed with a 3-median method. All the PDDs were normalized to their individual d_{max} values.

The irregular field was sketched by hand to simulate an electron boost treatment that is typically given to the scar where a breast tumor was removed. On average it had a 3.5 cm diameter, following a slight curve for about 11 cm. Figure 15 shows an image of the irregular cutout. As noted in Table 1, two measurements were made with the irregular cutout; one in the center and one in the corner.

Figure 15. The irregular cutout. The corner measurement was taken in the bottom right corner, indicated by the black dot.

Chapter 3

Results

3.1 σ_{1cm} vs σ_{2cm} Calculations

Graphs were produced of the measured and the calculated data. These were done separately for each pencil beam parameter. Figure 16 and Figure 17 show the difference of the measured and calculated data for σ_{1cm} and σ_{2cm}, respectively. The measured data for these two figures is from the 2 cm cutout.

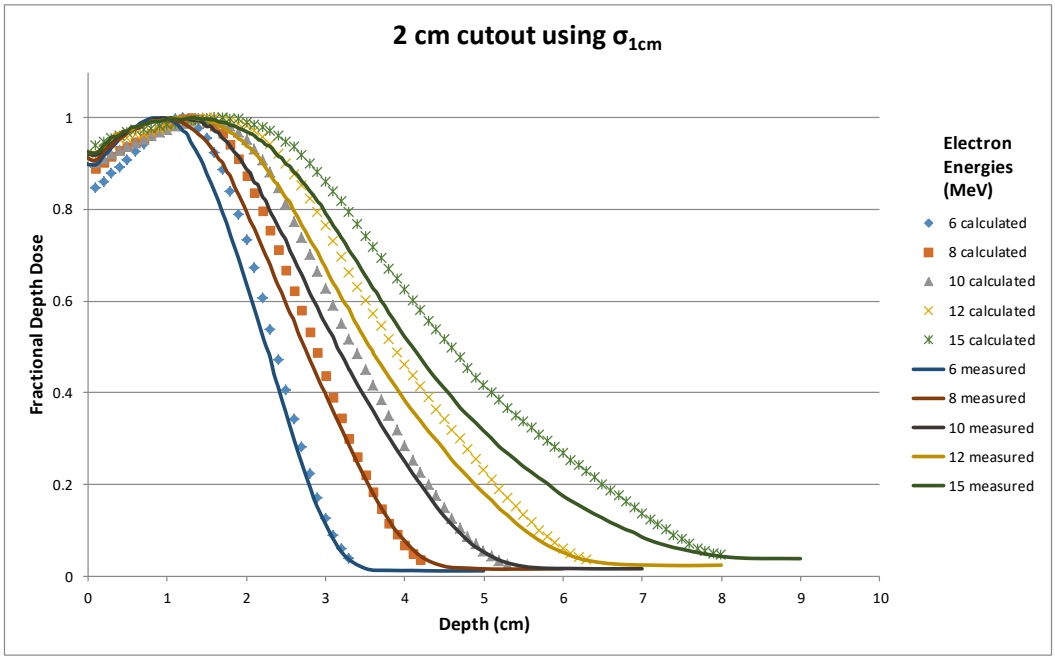

Figure 16. Profiles of measured and calculated data for the 2 cm cutout using the $\boldsymbol{\sigma_{1cm}}$.

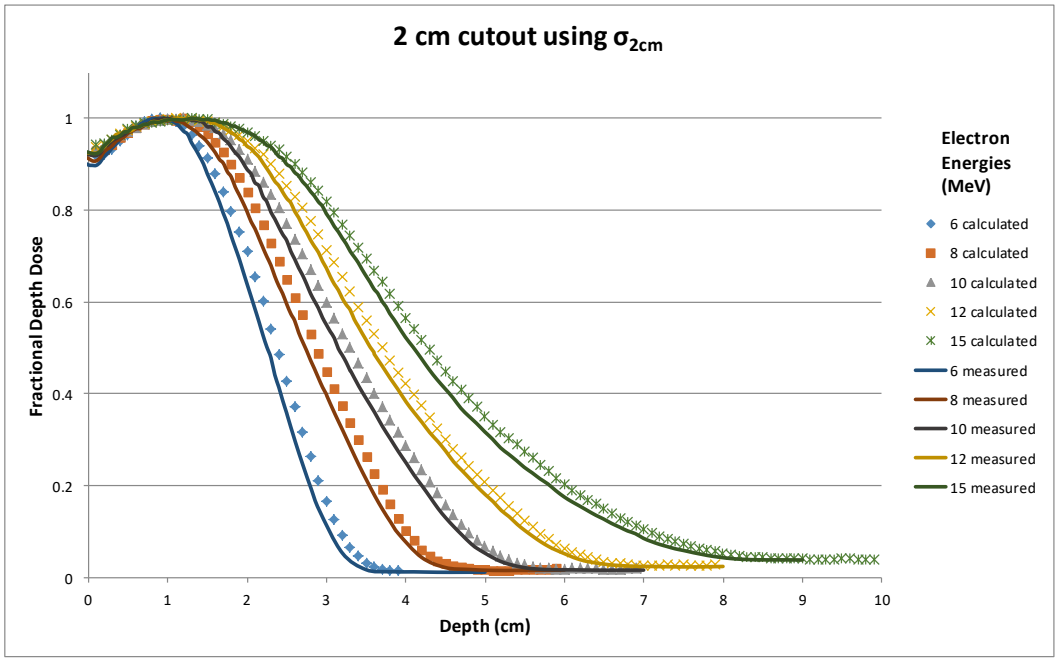

Figure 17. Profiles of measured and calculated data for the 2 cm cutout using the $\boldsymbol{\sigma_{2cm}}$.

The same graphs were also produced for the 3 cm cutout. These comparisons are displayed in Figure 18 and Figure 19.

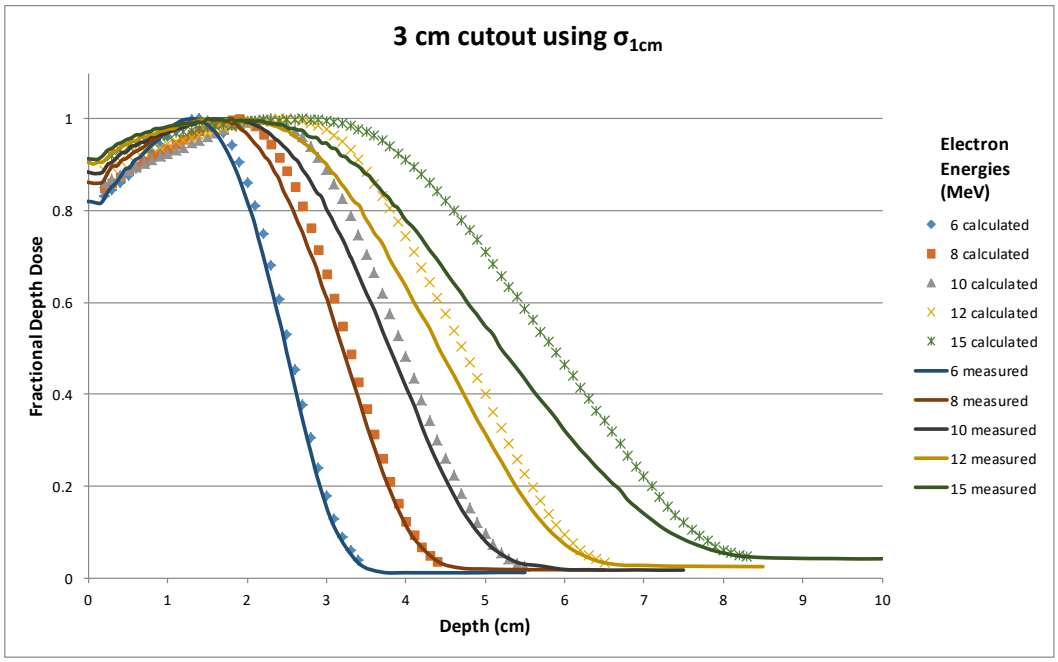

Figure 18. Profiles of measured and calculated data for the 3 cm cutout using the $\boldsymbol{\sigma_{1cm}}$.

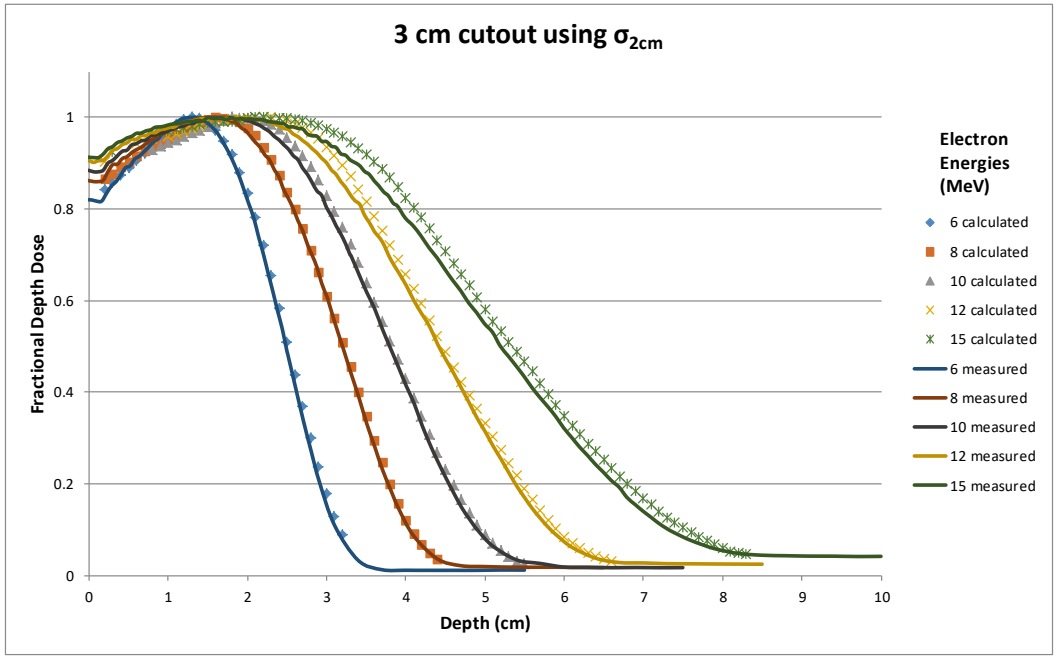

Figure 19. Profiles of measured and calculated data for the 3 cm cutout using the $\boldsymbol{\sigma_{2cm}}$.

Lastly, graphs comparing measured and calculated data from the irregular cutout measured from the center of the field are shown in Figure 20 and Figure 21.

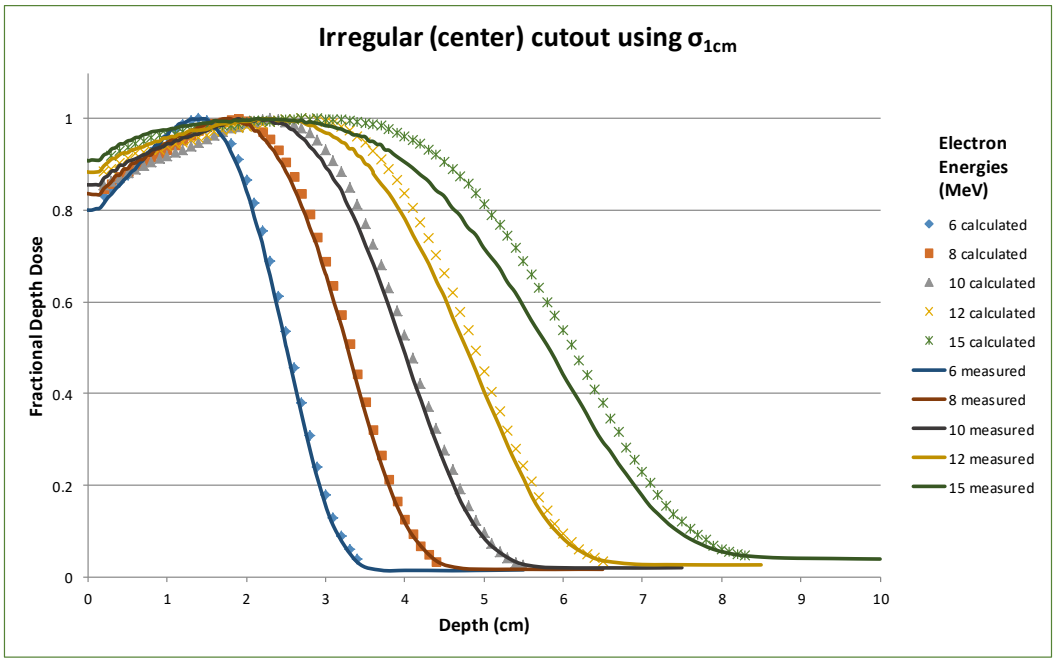

Figure 20. Profiles of measured and calculated data for the center of the irregular cutout using the $\boldsymbol{\sigma_{1cm}}$.

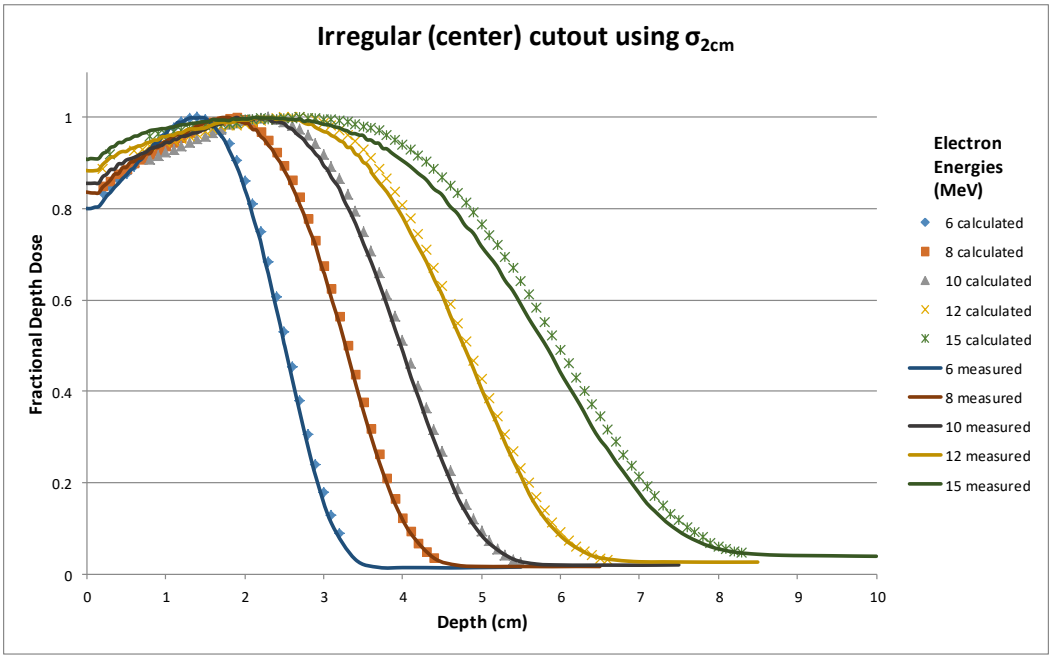

Figure 21. Profiles of measured and calculated data for the center of the irregular cutout using the $\boldsymbol{\sigma_{2cm}}$.

Figures 26 – 33 contain the rest of the graphs comparing measured vs calculated data for the cutouts and are shown in the Appendix.

3.2 d_{max}

The calculated profiles were compared to the measured profiles using the d_{max} depths. A tolerance of 0.5% of d_{max} was given due to the broad plateau exhibited by the larger electron energies.

From left to right, the columns of Table 2 are the radius required for LSE (R_{eq}), electron energies, cones sizes, and the cutouts measured. The d_{max} values from the measurements are shown in the yellow column. The last columns show the d_{max} calculations from σ_{1cm} and σ_{2cm}.

Table 2. The measured and calculated d_{max} values are compared. The yellow column is the measured range within 0.5% of d_{max}. Note that the field sizes are given as diameters.

			≥ R_{eq} = open	Plus or minus 0.5% of d_{max}	σ_{1cm} calculation of d_{max}		σ_{2cm} calculation of d_{max}	
R_{eq} (cm)	**Energy**	**Cone (cm^2)**	**Field size (cm)**	**d_{max} meas (cm)**	**Exact (cm)**	**Range (cm)**	**Exact (cm)**	**Range (cm)**
2.2	6 MeV	6	2	0.8 - 1	1.3	1.2 - 1.3	0.9	0.8 - 1
			4	1.2 - 1.5	1.4	1.3 - 1.5	1.4	1.3 - 1.5
			≥ R_{eq}	1.3 - 1.5	1.4	1.3 - 1.5	1.4	1.3 - 1.5
		10	3	1.2 - 1.4	1.4	1.3 - 1.4	1.3	1.2 - 1.4
			4	1.3 - 1.5	1.4	1.3 - 1.5	1.4	1.3 - 1.4
			8	1.2 - 1.5	1.4	1.3 - 1.5	1.4	1.3 - 1.5
		14	Irregular (ctr)	1.3 - 1.5	1.4	1.3 - 1.5	1.4	1.3 - 1.4
			Irregular (crn)	1.3 - 1.5	1.4	1.3 - 1.5	1.4	1.3 - 1.4
2.5	8 MeV	6	2	0.95 - 1	1.5	1.4 - 1.6	1.2	1.2
			4	1.6 - 1.9	1.9	1.8 - 2	1.9	1.8 - 1.2
			≥ R_{eq}	1.7 - 2	1.9	1.8 - 1.2	1.9	1.8 - 1.2
		10	3	1.4 - 1.8	1.9	1.8 - 1.9	1.6	1.5 - 1.8
			4	1.6 - 1.9	1.9	1.8 - 1.2	1.9	1.8 - 1.2
			8	1.6 - 1.9	1.9	1.8 - 1.2	1.9	1.8 - 1.2
		14	Irregular (ctr)	1.6 - 1.9	1.9	1.8 - 2	1.9	1.8 - 1.9
			Irregular (crn)	1.7 - 1.9	1.9	1.8 - 2	1.9	1.7 - 1.9
2.8	10 MeV	6	2	0.9 - 1.4	1.8	1.6 - 1.8	1.2	0.9 - 1.3
			4	1.8 - 2.3	2.3	2.2 - 2.4	2.3	2.2 - 2.4
			≥ R_{eq}	2.1 - 2.5	2.3	2.2 - 2.5	2.3	2.2 - 2.5
		10	3	1.5 - 1.9	2.3	2.1 - 2.4	1.8	1.8 - 2.1
			4	1.7 - 2.2	2.3	2.2 - 2.4	2.3	2.2 - 2.4
			8	2 - 2.5	2.3	2.2 - 2.5	2.3	2.2 - 2.5
		14	Irregular (ctr)	1.8 - 2.3	2.3	2.2 - 2.4	2.3	2.1 - 2.4
			Irregular (crn)	1.9 - 2.2	1.6	2.2 - 2.4	2.3	2 - 2.4
3.0	12 MeV	6	2	1 - 1.5	1.7	1.6 - 1.9	1.1	0.9 - 1.4
			4	1.9 - 2.4	2.7	2.4 - 3	2.7	2.3 - 2.9
			≥ R_{eq}	2.4 - 2.9	2.7	2.4 - 3	2.7	2.4 - 3
		10	3	1.4 - 2.1	2.5	2.3 - 2.7	2.2	1.8 - 2.4
			4	1.7 - 2.5	2.7	2.4 - 3	2.7	2.3 - 2.9
			8	2.4 - 3	2.7	2.4 - 3	2.7	2.4 - 3
		14	Irregular (ctr)	2.1 - 2.7	2.7	2.4 - 2.9	2.5	2.3 - 2.9
			Irregular (crn)	1.8 - 2.5	2.7	2.4 - 2.9	2.5	2.3 - 2.7
3.4	15 MeV	6	2	1 - 1.6	2.0	1.6 - 2.2	1.3	1 - 1.5
			4	1.5 - 2.4	2.7	2.1 - 3.3	2.7	2.1 - 3.1
			≥ R_{eq}	2.1 - 2.6	2.9	2.1 - 3.4	2.9	2.1 - 3.4
		10	3	1.5 - 2.2	2.7	2.1 - 3	2.2	1.2 - 2.6
			4	1.6 - 2.3	2.7	2.1 - 3.3	2.7	2.1 - 3.1
			8	2.4 - 3.2	2.9	2.1 - 3.4	2.9	2.1 - 3.4
		14	Irregular (ctr)	1.9 - 2.6	2.7	2.1 - 3.3	2.7	2.1 - 3.1
			Irregular (crn)	1.8 - 2.3	2.7	2.1 - 3.2	2.7	2.3 - 2.9

3.3 R_{90}

The original paper did not specify what location was used for clinically significant depths, but for this work the depth of R_{90} was chosen. Linear interpolation was verified to adequately model the profiles, as shown in Figure 22. This was necessary to extract the dose values at specific depths for comparison of the R_{90} locations and dose percentages.

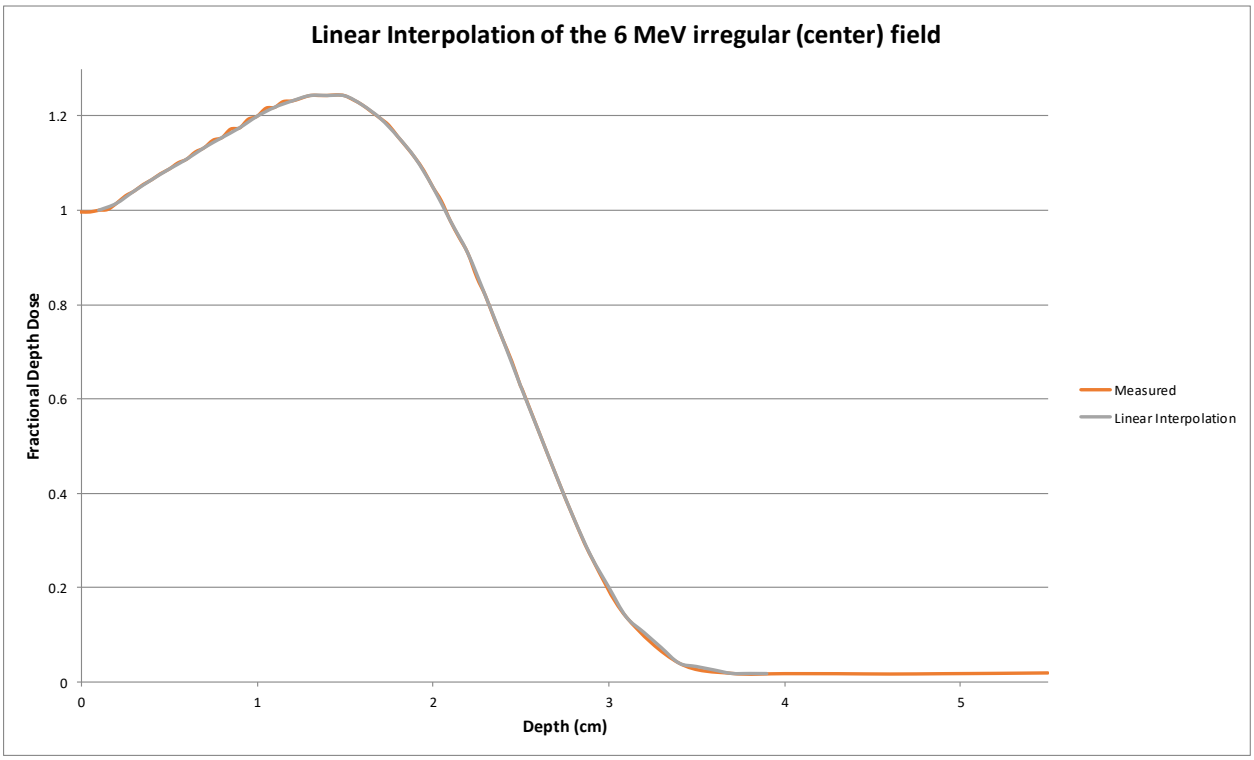

Figure 22. Verification of the linear interpolation. Shown is a full profile for a measured field, along with a profile after going through a linear interpolation reducing the data points to match the calculated data points.

Values for R_{90} were found for all the measured cutouts. These depths were then used to interpolate the calculated profiles to find what the calculated dose were at those depths. Similarly, the calculated profiles were interpolated to find the depths at where the calculated 90% dose

occurred. Comparison could then be done for the difference in distance as well as percent dose difference. These assessments are displayed in Tables 3 – 9.

Table 3. Comparing the $\boldsymbol{R_{90}}$ for the 2 cm cutout.

2 cm cutout						
Energy	Criteria	Measured	σ_{1cm} calculation	Difference	σ_{2cm} calculation	Difference
6 MeV	Distance	1.45 cm	1.77 cm	3.14 mm	1.54 cm	0.88 mm
	Dose	90%	98.51%	9.46%	92.68%	2.98%
8 MeV	Distance	1.71 cm	2.13 cm	4.24 mm	1.81 cm	1.00 mm
	Dose	90%	99.05%	10.05%	92.49%	2.77%
10 MeV	Distance	1.96 cm	2.43 cm	4.71 mm	2.04 cm	0.79 mm
	Dose	90%	98.59%	9.55%	91.93%	2.15%
12 MeV	Distance	2.21 cm	2.70 cm	4.86 mm	2.30 cm	0.87 mm
	Dose	90%	98.01%	8.90%	91.81%	2.01%
15 MeV	Distance	2.50 cm	3.11 cm	6.09 mm	2.61 cm	1.06 mm
	Dose	90%	98.09%	8.98%	91.74%	1.93%

Table 4. Comparing the $\boldsymbol{R_{90}}$ for the 3 cm cutout.

3 cm cutout						
Energy	Criteria	Measured	σ_{1cm} calculation	Difference	σ_{2cm} calculation	Difference
6 MeV	Distance	1.83 cm	1.91 cm	0.87 mm	1.85 cm	0.20 mm
	Dose	90%	93.32%	3.69%	90.79%	0.88%
8 MeV	Distance	2.30 cm	2.46 cm	1.57 mm	2.32 cm	0.21 mm
	Dose	90%	94.42%	4.91%	90.71%	0.79%
10 MeV	Distance	2.66 cm	2.96 cm	3.00 mm	2.77 cm	1.05 mm
	Dose	90%	96.60%	7.33%	92.42%	2.69%
12 MeV	Distance	3.00 cm	3.44 cm	4.36 mm	3.18 cm	1.73 mm
	Dose	90%	97.58%	8.43%	93.37%	3.74%
15 MeV	Distance	3.37 cm	4.07 cm	6.96 mm	3.63 cm	2.57 mm
	Dose	90%	98.03%	8.92%	93.69%	4.10%

Table 5. Comparing the R_{90} for the 4 cm cutout.

4 cm cutout (6 cone)						
Energy	Criteria	Measured	σ_{1cm} calculation	Difference	σ_{2cm} calculation	Difference
6 MeV	Distance	1.87 cm	1.92 cm	0.58 mm	1.92 cm	0.50 mm
	Dose	90%	92.30%	2.56%	91.97%	2.19%
8 MeV	Distance	2.46 cm	2.52 cm	0.61 mm	2.49 cm	0.24 mm
	Dose	90%	91.71%	1.90%	90.69%	0.77%
10 MeV	Distance	2.97 cm	3.14 cm	1.69 mm	3.05 cm	0.80 mm
	Dose	90%	94.01%	4.45%	92.14%	2.38%
12 MeV	Distance	3.40 cm	3.75 cm	3.43 mm	3.60 cm	1.97 mm
	Dose	90%	96.31%	7.01%	94.04%	4.49%
15 MeV	Distance	3.82 cm	4.53 cm	7.11 mm	4.24 cm	4.22 mm
	Dose	90%	97.72%	8.57%	95.72%	6.35%

Table 6. Comparing the R_{90} for the 4 cm cutout.

4 cm cutout (10 cone)						
Energy	Criteria	Measured	σ_{1cm} calculation	Difference	σ_{2cm} calculation	Difference
6 MeV	Distance	1.89 cm	1.92 cm	0.38 mm	1.92 cm	0.30 mm
	Dose	90%	91.59%	1.77%	91.25%	1.39%
8 MeV	Distance	2.43 cm	2.52 cm	0.94 mm	2.49 cm	0.57 mm
	Dose	90%	92.55%	2.83%	91.61%	1.79%
10 MeV	Distance	2.89 cm	3.14 cm	2.48 mm	3.05 cm	1.59 mm
	Dose	90%	95.60%	6.23%	94.04%	4.49%
12 MeV	Distance	3.29 cm	3.75 cm	4.56 mm	3.60 cm	3.10 mm
	Dose	90%	97.60%	8.45%	95.89%	6.54%
15 MeV	Distance	3.72 cm	4.53 cm	8.15 mm	4.24 cm	5.26 mm
	Dose	90%	98.50%	9.44%	96.89%	7.65%

Table 7. Comparing the R_{90} for the 8 cm cutout.

8 cm cutout						
Energy	Criteria	Measured	σ_{1cm} calculation	Difference	σ_{2cm} calculation	Difference
6 MeV	Distance	1.86 cm	1.92 cm	0.63 mm	1.92 cm	0.63 mm
	Dose	90%	92.46%	2.73%	92.46%	2.73%
8 MeV	Distance	2.48 cm	2.53 cm	0.43 mm	2.53 cm	0.43 mm
	Dose	90%	91.25%	1.39%	91.25%	1.39%
10 MeV	Distance	3.07 cm	3.18 cm	1.09 mm	3.18 cm	1.09 mm
	Dose	90%	92.43%	2.70%	92.43%	2.70%
12 MeV	Distance	3.73 cm	3.84 cm	1.13 mm	3.84 cm	1.13 mm
	Dose	90%	92.23%	2.47%	92.23%	2.47%
15 MeV	Distance	4.53 cm	4.68 cm	1.49 mm	4.68 cm	1.49 mm
	Dose	90%	92.07%	2.30%	92.07%	2.30%

Table 8. Comparing the R_{90} for the irregular cutout.

Irregular (center) cutout						
Energy	Criteria	Measured	σ_{1cm} calculation	Difference	σ_{2cm} calculation	Difference
6 MeV	Distance	1.88 cm	1.92 cm	0.45 mm	1.91 cm	0.35 mm
	Dose	90%	91.81%	2.01%	91.41%	1.56%
8 MeV	Distance	2.45 cm	2.52 cm	0.64 mm	2.49 cm	0.33 mm
	Dose	90%	91.78%	1.97%	90.92%	1.02%
10 MeV	Distance	2.98 cm	3.14 cm	1.52 mm	3.07 cm	0.88 mm
	Dose	90%	93.62%	4.02%	92.27%	2.52%
12 MeV	Distance	3.52 cm	3.75 cm	2.30 mm	3.65 cm	1.25 mm
	Dose	90%	94.37%	4.85%	92.58%	2.87%
15 MeV	Distance	4.04 cm	4.54 cm	4.97 mm	4.32 cm	2.80 mm
	Dose	90%	95.83%	6.47%	93.59%	3.99%

Table 9. Comparing the R_{90} for the irregular cutout.

Irregular (corner) cutout						
Energy	Criteria	Measured	σ_{1cm} calculation	Difference	σ_{2cm} calculation	Difference
6 MeV	Distance	1.86 cm	1.92 cm	0.61 mm	1.91 cm	0.44 mm
	Dose	90%	92.37%	2.64%	91.67%	1.86%
8 MeV	Distance	2.41 cm	2.51 cm	0.98 mm	2.46 cm	0.44 mm
	Dose	90%	92.69%	2.98%	91.30%	1.44%
10 MeV	Distance	2.92 cm	3.11 cm	1.87 mm	3.01 cm	0.93 mm
	Dose	90%	94.47%	4.96%	92.42%	2.69%
12 MeV	Distance	3.37 cm	3.69 cm	3.15 mm	3.53 cm	1.59 mm
	Dose	90%	95.87%	6.53%	93.18%	3.53%
15 MeV	Distance	3.83 cm	4.45 cm	6.24 mm	4.13 cm	3.05 mm
	Dose	90%	97.04%	7.82%	94.26%	4.73%

Chapter 4

Discussion

4.1 σ_{1cm} vs σ_{2cm} Calculations

It is apparent that both pencil beam calculations result in an overestimation of the true PDD. This effect has also been noted by other investigators, and is attributed to the fact that only one pencil beam parameter is used.[5] This trend is true for all depths, energies, and cutouts measured in this study. The comparison between Figure 16 and Figure 17 is inherently biased for the σ_{2cm} calculation because the original measurement for σ_{2cm} stems from a 2 cm cutout. Thus it would be expected that the σ_{2cm} calculation would give better results. However, analyzing Figure 18 and Figure 19 shows that the calculations from σ_{2cm} better match the measured data. This trend of σ_{2cm} calculations yielding better results to measurements than σ_{1cm} was found for every cutout.

4.2 d_{max} Comparison

From Table 2, the exact d_{max} did not fall into the measured range 19 out of 40 times for the σ_{1cm}. Meanwhile for the σ_{2cm}, it did not fall into the range 11 out of 40 times. The majority of these occurrences were in the higher electron energies, 12 and 15 MeV. The σ_{1cm} never met the measured d_{max} range for the smallest cutout of 2 cm.

4.3 R_{90} Comparison

From a pragmatic viewpoint of clinical setup, the limit for dose deviance at R_{90} is 3%. Using this as standard it is apparent that the σ_{1cm} calculations are not adequate. The σ_{1cm} calculation is up to 9% of the measured dose for the 2 cm cutout, and the distance is greater than 3 mm for all energies. Contrast these values to the σ_{2cm} calculation which is barely exceeding 1 mm difference and stays under 3% for all energies. This pattern of the σ_{1cm} calculations being worse is exhibited in all cutouts. The calculations from the σ_{2cm} parameter do well for lower energies. However, even for energies above 10 MeV the percent dose difference starts to exceed 3%. Most of the distances are below 3 mm, with the exception of the 4 cm cutout for 12 and 15 MeV. Notice for the 8 cm cutout both the calculations are the same. This is because the LBR for the 8 cm is essentially one at all depths, reducing Equation 8 down to the cone factor multiplied by the open PDD.

Differences of the calculation versus measured for the same cutout but different cone sizes was observed. Better prediction for the 6 MeV with the larger cone (10 cm^2) was found. Also, better prediction was found for the higher energies (>6 MeV) with the smaller 6 cm^2 cone. Smaller cones have been found to introduce more low-energy scatter. Comparatively, bigger cones have deeper PDDs.[29] Thus it would have been assumed, due to overestimation of the PDDs with the LBR, that the bigger cone would give better prediction for all energies. Further investigation is required to make a definitive statement as only two cone sizes for the same cutout were compared in this study.

4.4 Investigation of the LBR

The LBRs were plotted against the depths when normalized to the practical range, R_p. These are shown in Figure 23 and Figure 24.

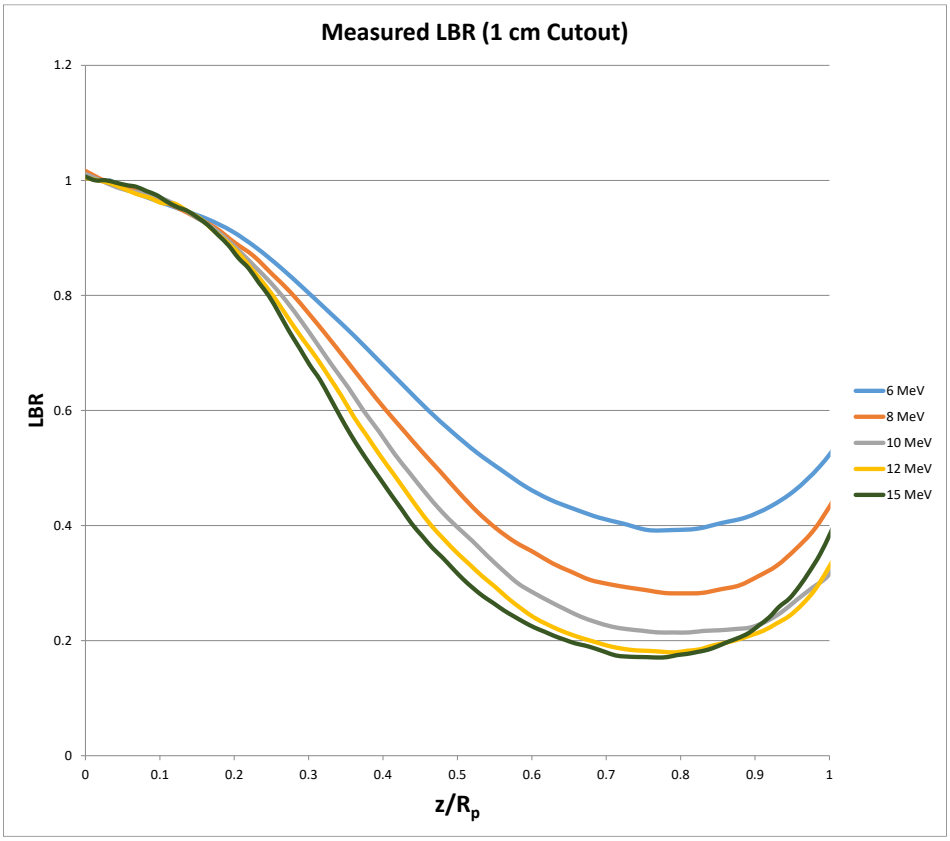

Figure 23. The measured LBR from the 1 cm cutout is plotted against the depth normalized to the practical range for all 5 electron energies.

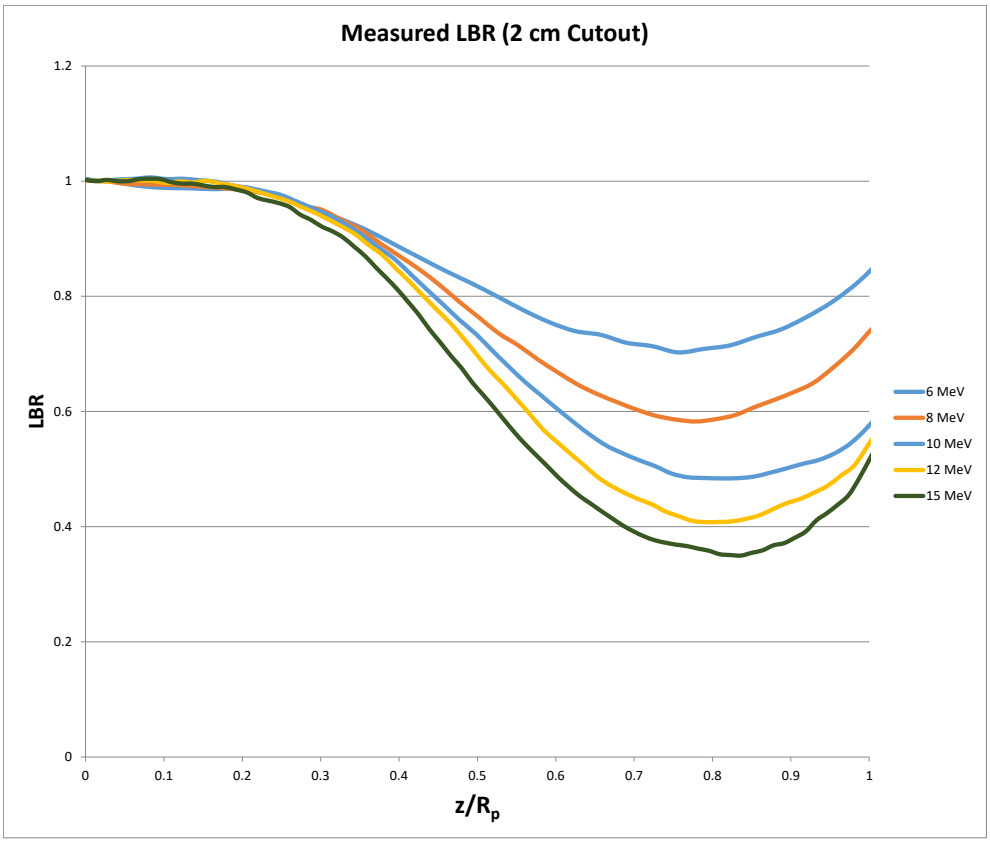

Figure 24. The measured LBR from the 2 cm cutout is plotted against the depth normalized to the practical range for all 5 electron energies.

These figures show that the LBR near the surface are nearly the same for all energies and for both the cutouts. This ensures that the normalization of the data at the 0.983 mm depth is sufficient to factor out the fluence terms that are present in Equation 3.

Due to the fact that two LBRs were being measured for this study, the two pencil beams derived from the LBRs could also be plotted against the depth normalized to the practical range. This is shown in Figure 25.

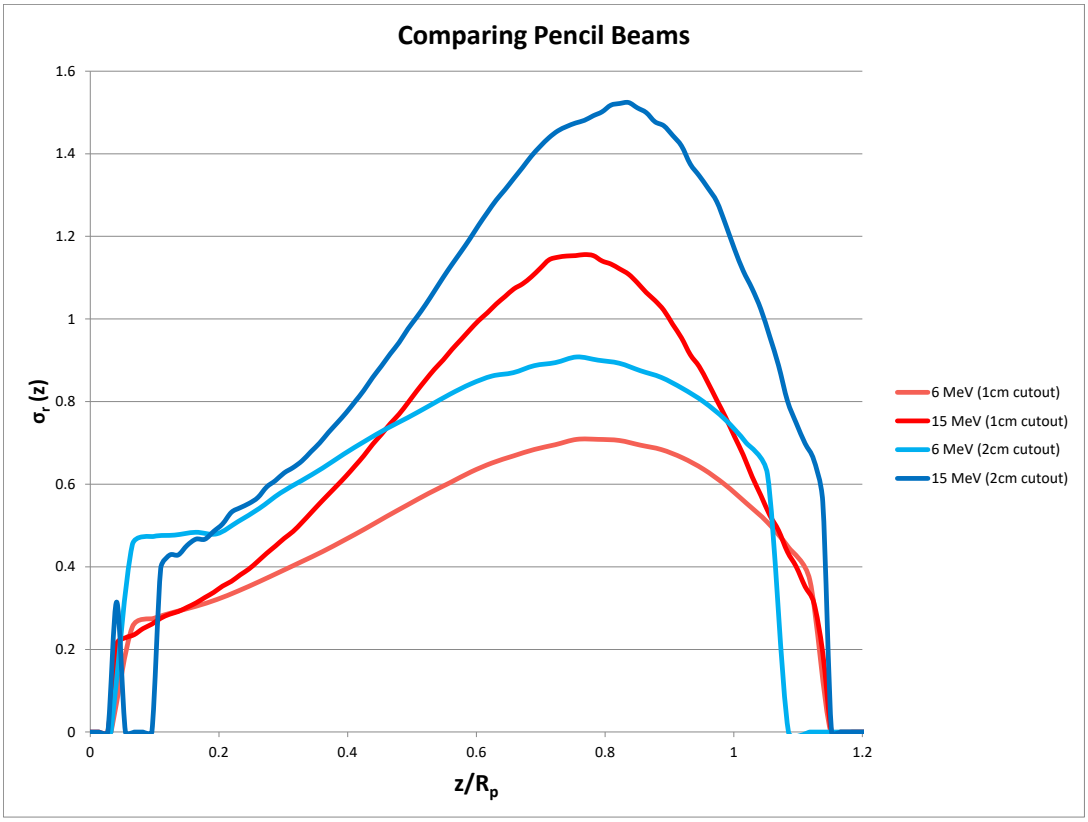

Figure 25. The pencil beam parameters are both plotted against the depth normalized to $\boldsymbol{R_p}$ for 6 and 15 MeV. The red colors are from the 1 cm cutout, and the blue from the 2 cm cutout.

The σ_{1cm} and σ_{2cm} pencil beam parameters show a dramatic difference in their maximum spread, which occurs around 0.7 of the normalized depth. This is shown for both 6 and 15 MeV. In the original paper, a similar plot is made for field sizes of 2, 2.8, and 3.7 cm for 9 MeV. Some differences are noted and suspected to be from scatter in the measured data and changes in the initial angular spread of the pencil beams. The paper concludes that these differences on the depth dose curves is limited to 3%.[1] Gebreamlak et al investigated more field sizes, up to 6 cm for 15 MeV. This showed a variation in the pencil beam parameter of about 1.55 for the 2 cm cutout to 1.7 for the 6 cm cutout.[5] This investigation of the 1 cm also exhibits a dependence of the pencil beams on field size. The difference seen in Figure 25 is much more extreme and varies the pencil beam from 1.15 to 1.5 for the 15 MeV beam. This not only further concludes that the pencil beam

parameter does depend on field size, but also shows that the LBR method is more of an empirical formulation and the theory of the LBR method might have limitations.

Chapter 5

Conclusions

5.1 Study Limitations

An improvement for this study would be the use of a 3D scanner, especially for the measurement of the LBR. This would enable one to more confidently verify that the detector is at the center of the cutout at all depths.

Another limitation to this study was the amount of time available. Extending this study with another graduate student would allow for further investigation and implementation of the improvements of the LBR proposed by other authors.[5,6]

5.2 Future Work

It has been mentioned that Gebreamlak et al[5] have investigated the addition of using varying pencil beam parameters found via interpolation of $\sigma_r(z)$ vs. R curves to predict even better calculations. It would be prudent to investigate the interpolation of the pencil beam parameter and use different $\sigma_r(z)$ for varying radii in an irregular field as an improvement to this study.

Increasing the dwell times and decreasing the point spacing of the initial measurements for the LBR might be an area of investigation. This might help the LBR's uncertainty at shallow depths and produce less uncalculated data points of the LBR. Some of the calculations for shallow depths produced errors. This is because of the sensitivity near the surface, as well as the dose from the

small cutout and the open field being relatively the same. Taking finer measurements might result in less errors in the near surface.

Streamlining the calculations of fields could also be done in VBA. For the purposes of this thesis, the calculations were done in the Excel main interface. Coding this into VBA or even another program would enable for quick calculations. Another area of interest would be to set up an automated way to load in an image or sketch of an irregular field and have the radii extend automatically to the boundaries. Having this would make for an efficient calculation of an irregular field.

Another area of future investigation would be altering the number of sectors used for the sector integration of the irregular fields. Changing this would have an impact for how accurate the calculations are, while also trying to balance what is sufficient for the LBR method. Implementing a feature of selecting how many segments one would want to use for the sector integration of the irregular field would enable a study into varying sector amounts.

5.2 Final Conclusions

From this work it can be concluded that the 1 cm cutout used to measure the LBR results in calculations that are not as accurate when compared to the 2 cm cutout calculations. This result was true for both the d_{max} and R_{90} comparisons. It is further concluded that the LBR method should not be used for energies above 10 MeV. Even when lower energies are considered, the application of this method should be used cautiously as the calculation tends to always overestimate the true electron PDD. As mentioned in 5.2, Gebreamlak et al[5] have explored the use of varying pencil beam parameters found via interpolation of $\sigma_r(z)$ vs. R curves to predict better calculations. Serious consideration of this paper should be taken into account when seeking to

implement this clinically. In conclusion, this study has shown that the 1 cm cutout used for the LBR measurement does not produce accurate results, and that the LBR method as originally introduced should not be used for energies above 10 MeV.

References

1. Khan FM, Higgins PD, Gerbi BJ, Deibel FC, Sethi A, Mihailidis DN. Calculation of depth dose and dose per monitor unit for irregularly shaped electron fields. *Phys Med Biol*. 1998;43(10):2741–2754. doi:10.1088/0031-9155/43/10/005

2. McParland BJ. A method of calculating the output factors of arbitrarily shaped electron fields. *Med Phys*. 1989;16(1):88-93. doi:10.1118/1.596366

3. Tyner E, McCavana P, McClean B. A modified method of calculating the lateral build-up ratio for small electron fields. *Phys Med Biol*. 2006;51(12):N241–N246. doi:10.1088/0031-9155/51/12/N02

4. Jursinic PA, Mueller R. A sector-integration method for calculating the output factors of irregularly shaped electron fields. *Med Phys*. 1997;24(11):1765-1769. doi:10.1118/1.597962

5. Gebreamlak WT, Tedeschi DJ, Alkhatib HA. Dose calculation for electron therapy using an improved LBR method. *Med Phys*. 2013;40(7):071717. doi:10.1118/1.4810938

6. Alkhatib HA, Gebreamlak WT, Tedeschi DJ, et al. Output calculation of electron therapy at extended SSD using an improved LBR method. *Med Phys*. 2015;42(2):735-740. doi:10.1118/1.4905375

7. Kehwar TS, Huq MS. The root percent depth dose method for calculating monitor units for irregularly shaped electron fields. *Med Phys*. 2008;35(4):1214-1222. doi:10.1118/1.2868761

8. *Cancer Facts & Figures 2019*. Atlanta: American Cancer Society; 2019. https://www.cancer.org/research/cancer-facts-statistics/all-cancer-facts-figures/cancer-facts-figures-2019.html.

9. Khan FM, Gibbons JP. *Khan's The Physics of Radiation Therapy*. 5th ed. Philadelphia, PA: Lippincott Williams & Wilkins/Wolters Kluwer; 2014. https://shop.lww.com/Khan-s-The-Physics-of-Radiation-Therapy/p/9781451182453. Accessed April 12, 2019.

10. Laughlin JS. Development of the Technology of Radiation Therapy. *Radiographics*. 1989;9(6):1245-1266.

11. Antolak JA, Hogstrom KR. Electron Radiotherapy Past, Present & Future. Presented at the: AAPM Annual Meeting; August 8, 2013; Indianapolis, IN.

12. Willett CG, Del Castillo CF, Shih HA, et al. Long-term Results of Intraoperative Electron Beam Irradiation (IOERT) for Patients With Unresectable Pancreatic Cancer. *Ann Surg*. 2005;241(2):295-299. doi:10.1097/01.sla.0000152016.40331.bb

13. Barney BM, Petersen IA, Dowdy SC, Bakkum-Gamez JN, Klein KA, Haddock MG. Intraoperative Electron Beam Radiotherapy (IOERT) in the management of locally advanced or recurrent cervical cancer. *Radiat Oncol*. 2013;8(1):80. doi:10.1186/1748-717X-8-80

14. Van de Graaff RJ, Trump JG. Method of and Apparatus for Electrostatically Generating Direct Current Power. March 1940:1-6. https://patentimages.storage.googleapis.com/9e/27/23/78b370123d15d0/US2194839.pdf. Accessed April 12, 2019.

15. Trump JG, Van de Graaff RJ, Cloud RW. Cathode Rays for Radiation Therapy. *Am J Roentgenol*. 1940;43:728-734.

16. Hare HF, Fromer JL, Trump JG, Wright KA, Anson JH. Cathode Ray Treatment For Lymphomas Involving The Skin. *AMA Arch Dermatol Syphilol*. 1953;68(6):635-642. doi:10.1001/archderm.1953.01540120019004

17. Hass LL, Laughlin JS, Harvey RA. Biological Effectiveness of High-Speed Electron Beam in Man. *Radiology*. 1954;62(6):845-851. doi:10.1148/62.6.845

18. Karzmark CJ, Nunan CS, Tanabe E. *Medical Electron Accelerators*. McGraw Hill, Inc.; 1993.

19. Biggs PJ, Boyer AL, Doppke KP. Electron dosimetry of irregular fields on the clinac 18. *Int J Radiat Oncol*. 1979;5(3):433-440. doi:10.1016/0360-3016(79)91228-8

20. Hogstrom KR, Boyer AL, Shiu AS, et al. Design of metallic electron beam cones for an intraoperative therapy linear accelerator. *Int J Radiat Oncol*. 1990;18(5):1223-1232. doi:10.1016/0360-3016(90)90461-R

21. Kassaee A, Altschuler MD, Ayyalsomayajula S, Bloch P. Influence of cone design on the electron beam characteristics on clinical accelerators. *Med Phys*. 1994;21(11).

22. Khan FM, Doppke KP, Hogstrom KR, et al. Clinical electron-beam dosimetry: Report of AAPM Radiation Therapy Committee Task Group No. 25. *Med Phys*. 1991;18(1):73-109. doi:10.1118/1.596695

23. Khan FM, Higgins PD. Field equivalence for clinical electron beams. *Phys Med Biol*. 2000;46(1):N9–N14. doi:10.1088/0031-9155/46/1/402

24. Procedures in External Radiation Therapy Dosimetry with Electron and Photon Beams with Maximum Energies Between 1 and 50 MeV Recommendations by the Nordic Association of Clinical Physics (NACP). *Acta Radiol Oncol*. 1980;19(1):55-79. doi:10.3109/02841868009130136

25. Xu Z, Walsh SE, Telivala TP, Meek AG, Yang G. Evaluation of the eclipse electron Monte Carlo dose calculation for small fields. *J Appl Clin Med Phys*. 2009;10(3):75-85. doi:10.1120/jacmp.v10i3.2834

26. Perry DJ, Holt JG. A model for calculating the effects of small inhomogeneities on electron beam dose distributions. *Med Phys*. 1980;7(3):207-215. doi:10.1118/1.594687

27. Hogstrom KR, Mills MD, Almond PR. Electron beam dose calculations. *Phys Med Biol*. 1981;26(3):445–459. doi:10.1088/0031-9155/26/3/008

28. Varadhan, Way S, Arentsen L, Gerbi B. SU-F-T-74: Experimental Validation of Monaco Electron Monte Carlo Dose Calculation for Small Fields. *Med Phys*. 2016;43(6Part13):3478-3478. doi:10.1118/1.4956210

29. Shiu AS, Tung SS, Nyerick CE, et al. Comprehensive analysis of electron beam central axis dose for a radiotherapy linear accelerator. *Med Phys*. 1994;21(4):559-566. doi:10.1118/1.597313

30. Taherkhani A, Mohammadi DM, Saboori MS, Changizi V. Evaluation of the physical characteristic of Cerrobend blocks used for radiation therapy. *Iran J Radiat Res*. 2010;8(2):10.

31. 1D Scanner Reference Guide. Sun Nuclear Corporation. https://www.sunnuclear.com/solutions/dosimetry/1dscanner. Published 2016. Accessed April 13, 2019.

32. Ionizing Radiation Detectors. PTW. https://www.ptw.de/fileadmin/data/download/catalogviewer/DETECTORS_Cat_en_16522900_11/blaetterkatalog/blaetterkatalog/pdf/complete.pdf. Published 2019. Accessed May 13, 2019.

Appendix A:

A.1 Graphs

The following are the rest of the graphs comparing measured to calculated data.

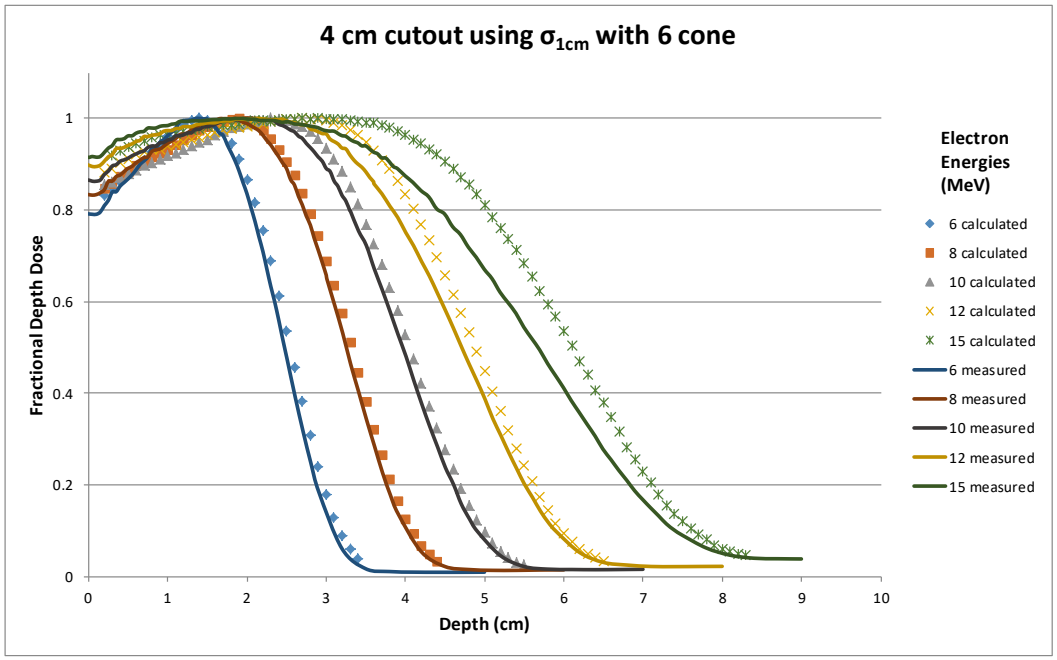

Figure 26. Profiles of measured and calculated data for the 4 cm cutout in the 6 cone using the σ_{1cm}.

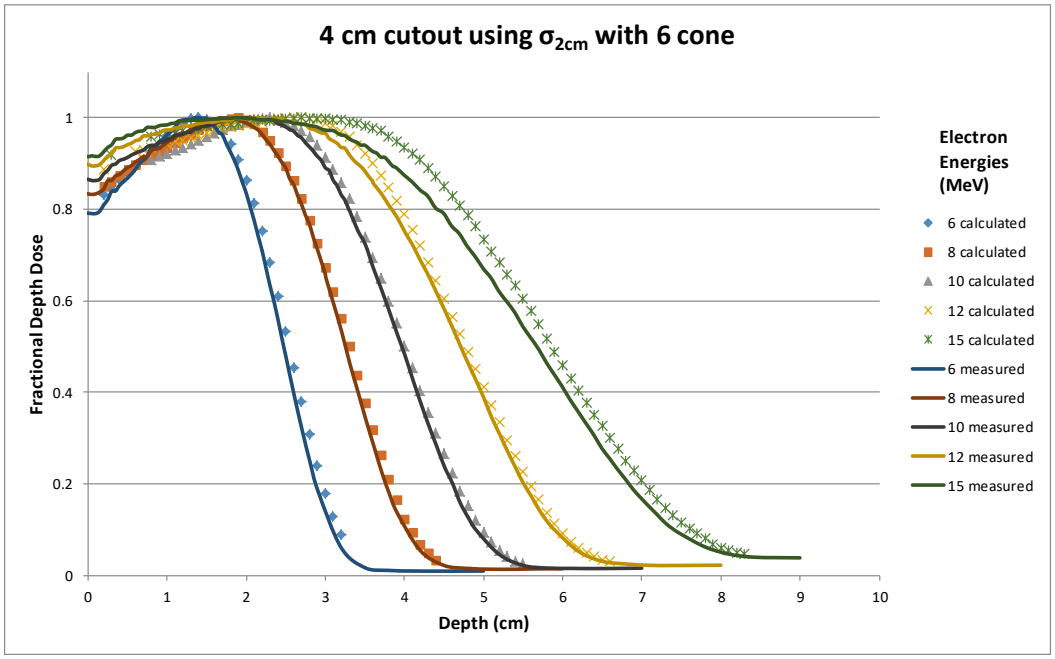

Figure 27. Profiles of measured and calculated data for the 4 cm cutout in the 6 cone using the σ_{2cm}.

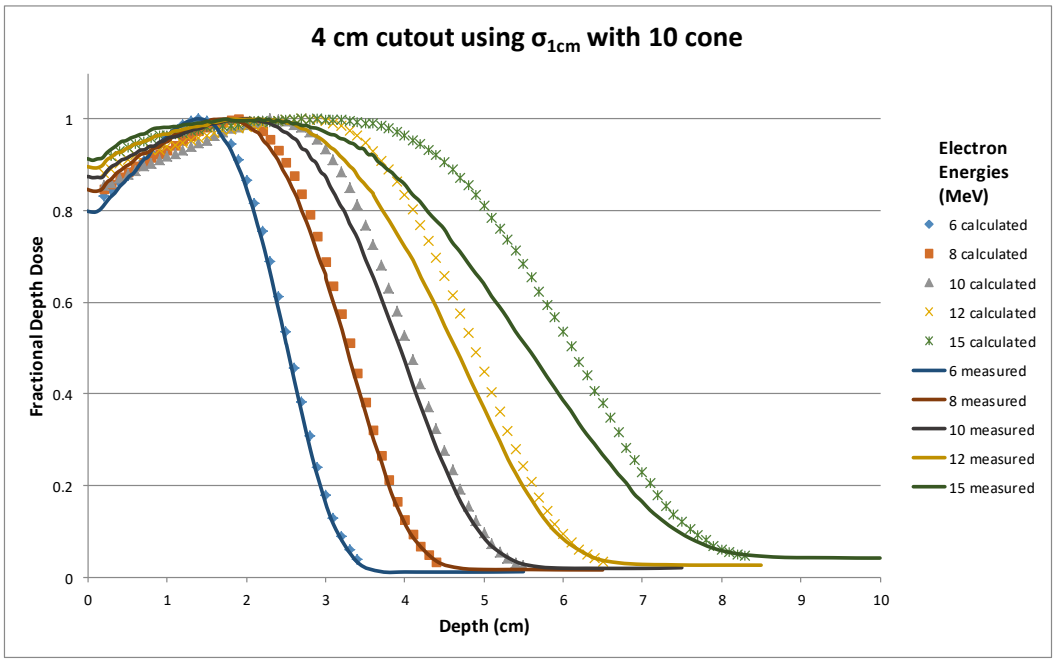

Figure 28. Profiles of measured and calculated data for the 4 cm cutout in the 10 cone using the σ_{1cm}.

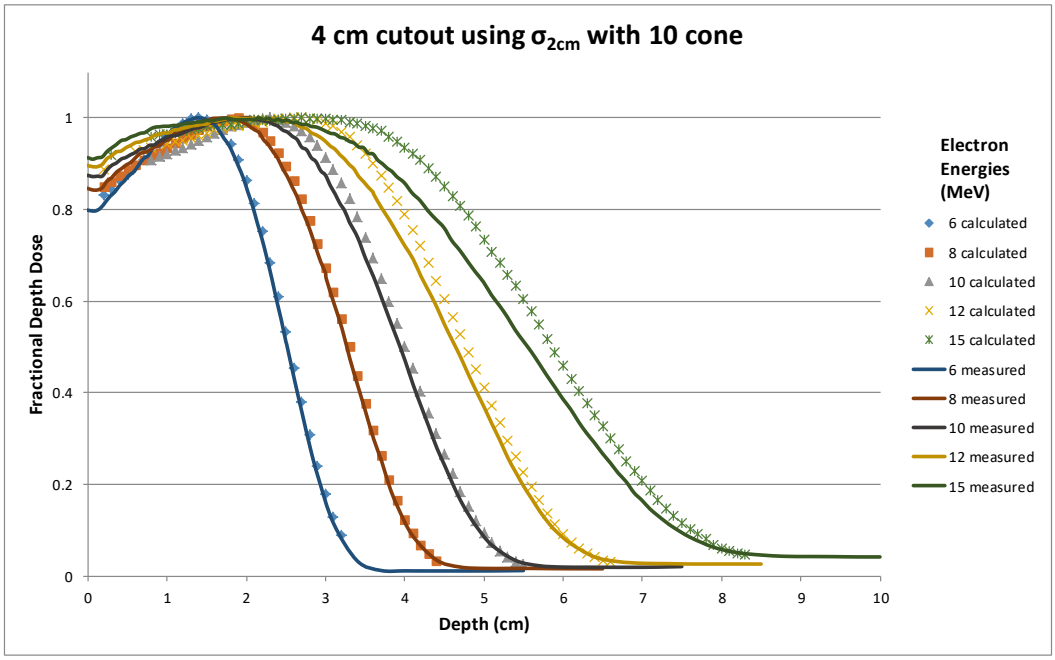

Figure 29. Profiles of measured and calculated data for the 4 cm cutout in the 10 cone using the $\boldsymbol{\sigma_{2cm}}$.

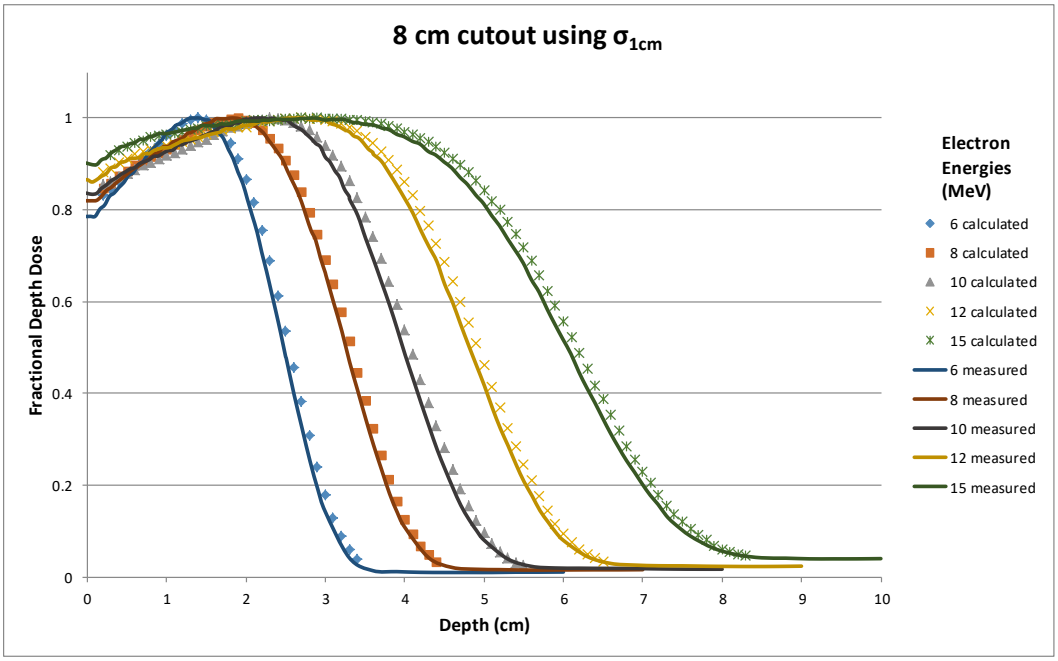

Figure 30. Profiles of measured and calculated data for the 8 cm cutout using the $\boldsymbol{\sigma_{1cm}}$.

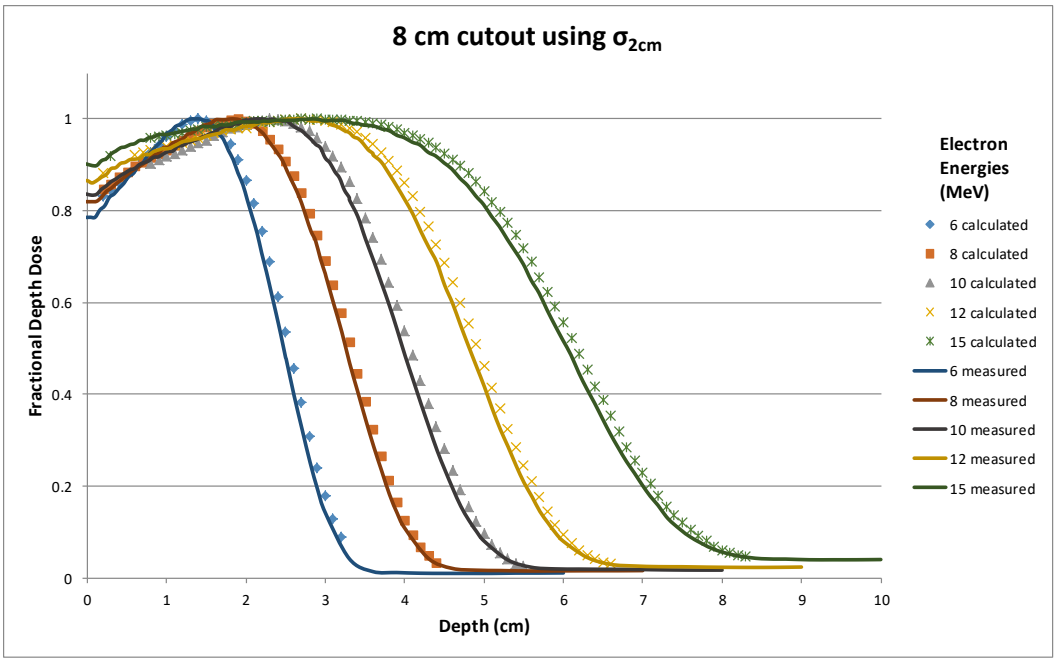

Figure 31. Profiles of measured and calculated data for the 8 cm cutout using the $\boldsymbol{\sigma_{2cm}}$.

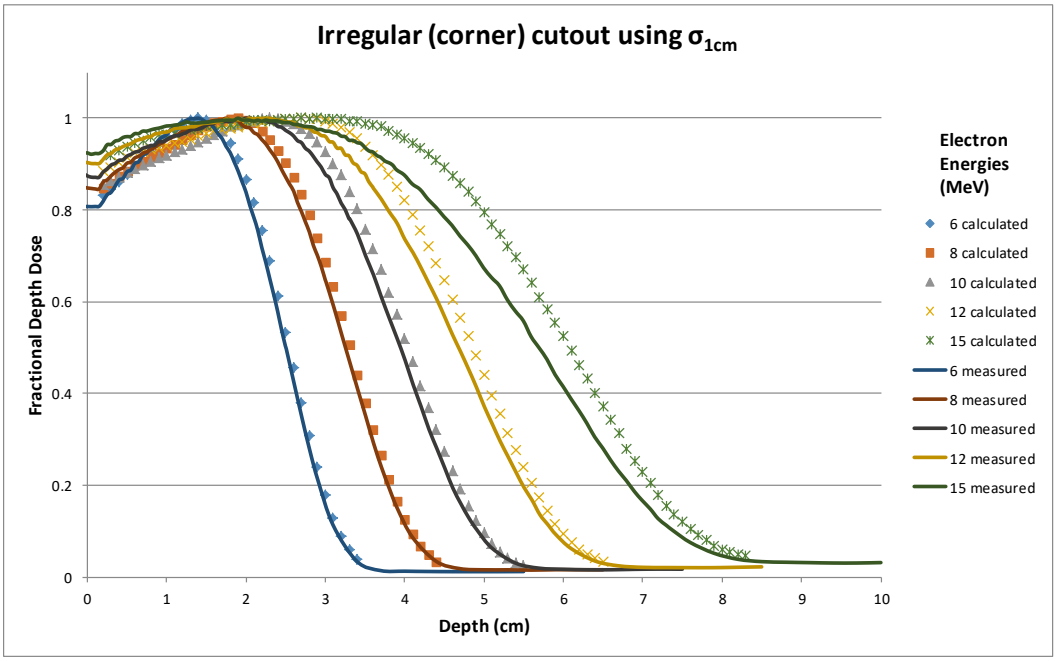

Figure 32. Profiles of measured and calculated data for the corner of the irregular cutout using the $\boldsymbol{\sigma_{1cm}}$.

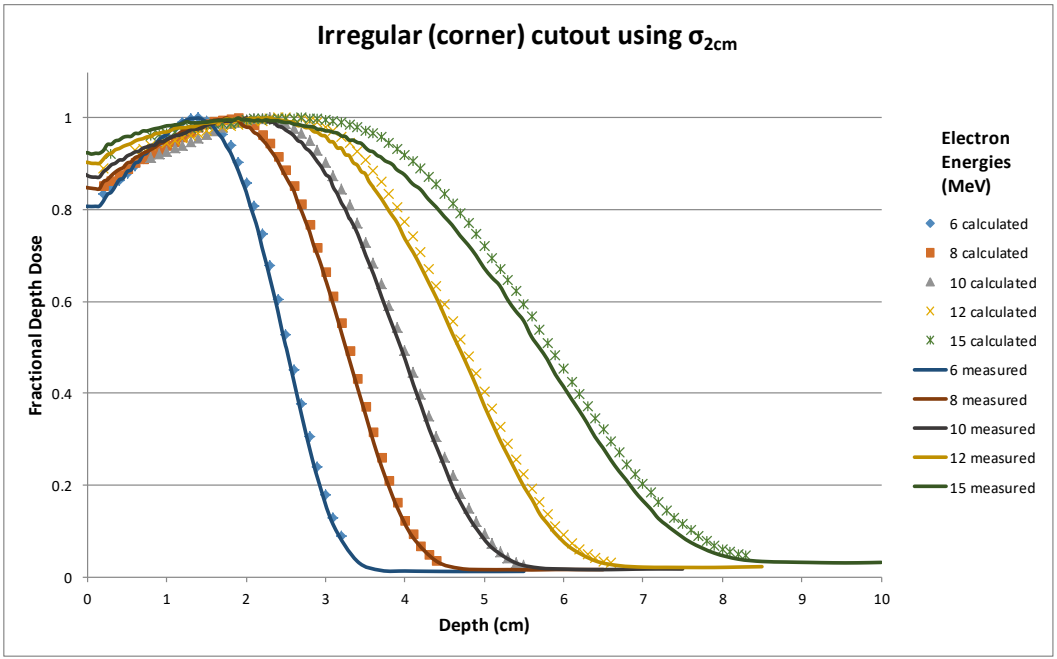

Figure 33. Profiles of measured and calculated data for the corner of the irregular cutout using the $\boldsymbol{\sigma_{2cm}}$.